ORIGINAL RESEARCH ARTICLE

Effects of Direct Aging Heat Treatments on the Superelasticity of Nitinol Produced *via* Laser Powder Bed Fusion

MARIA BEATRICE ABRAMI, MARIALAURA TOCCI, DERMOT BRABAZON, MARCELLO CABIBBO, and ANNALISA POLA

This work investigates the effects of short-time direct aging heat treatments on the mechanical properties and microstructure of additively manufactured Nitinol (NiTi) alloy. Cylindrical samples were produced through laser powder bed fusion (L-PBF), directly aged at different temperatures and compared to the solution annealed and aged conditions. Compression tests were carried out at room temperature both in cyclic mode at constant strain and incremental cyclic mode, to provide a comprehensive analysis on the superelastic features of NiTi after direct aging heat treatments. Furthermore, cyclic compression tests were performed at 37 °C to evaluate the superelastic effect at the body temperature and, therefore, the possibility to use these treatments for biomedical components. The effects of direct aging on the microstructure were characterized using transmission electron microscopy (TEM). High cyclic stability and superelastic recovery up to 10 pct of deformation emerged for the direct aged alloys. The comparable results obtained with and without the solution treatment points out that this step was not necessary in reaching superelasticity, proving the effectiveness of direct aging.

https://doi.org/10.1007/s11661-024-07513-6

I. INTRODUCTION

NITINOL (NiTi) alloy is commonly known as the most used shape memory metallic material, whose properties are exploited in many biomedical and engineering applications.[1–3] Its peculiar features, *i.e.* shape memory effect (SME) and superelasticity (SE), are related to the reversible transformation between martensite (M) and austenite (A).[4] The effect exhibited at the working temperature depends on the phase present, which is determined by the relative relationship between the transformation temperatures (TTs) and the working temperature. Therefore, for the obtainment of the desired properties the control of the TTs is crucial and is usually done by calibrating the chemical composition, as TTs are sensibly affected by the content of Ni and Ti. In fact, the 1 pct variation in the Ni content can lead to a change in the martensite starting temperature (M_s) of about 100 °C.[5] Another common way to tailor and improve NiTi behavior is through heat treatments, whose parameters need to be carefully selected based on the microstructure of components after the manufacturing process and on the application for which they are intended.

Several studies currently focus on the possibility to produce NiTi biomedical devices by additive manufacturing (AM) techniques, also due to the difficulties involved in their conventional production route, which arise from NiTi low machinability.[6] Among the AM methods, laser powder bed fusion (L-PBF) is preferred, due to the resulting finer microstructure and the better surface finish, both leading to higher performances.[7–9] The obtainment of SE is required for most of the NiTi biomedical components, especially for endovascular surgery (*e.g.* stents), and is commonly achieved through heat treatments. For conventionally produced Ni-rich components, it is well known that performing solution treatment followed by aging in the range of 400 °C to 600 °C enhances SE.[3,10–13]

Due to the differences between conventional and AM manufacturing methods, a lot of studies are aimed at determining the optimal heat treatments for AM parts,[13–22] based on the features of the as-built

MARIA BEATRICE ABRAMI, MARIALAURA TOCCI, and ANNALISA POLA are with the Department of Mechanical and Industrial Engineering, University of Brescia, Via Branze 38, 25123 Brescia, Italy. Contact e-mail: m.abrami003@unibs.it DERMOT BRABAZON is with the I-Form, Advanced Manufacturing Research Centre, School of Mechanical and Manufacturing Engineering, Dublin City University, Dublin, Ireland. MARCELLO CABIBBO is with the Department of Industrial Engineering and Mathematic Sciences (DIISM), Università Politecnica delle Marche, via Brecce Bianche 12, 60131 Ancona, Italy.
Manuscript submitted October 25, 2023; accepted July 2, 2024.
Article published online July 24, 2024

components, which in turn strongly depend on the powder chemical composition and on the process parameters used. Concerning the L-PBF technique, one of the main differences with the traditional methods consists in the higher possibility to run into Ni evaporation during the process, which can occur due to the high temperatures arising from the laser.[5,23] This leads to a variation of the chemical composition in the manufactured part compared to the starting powder and thus affects the properties of the component. In addition, L-PBF may generate different microstructures due to the non-equilibrium solidification process resulting from the complex thermal history involved.[24]

Despite the numerous studies focused on heat treatments after L-PBF,[17–22] only a few involve performing aging without prior solution annealing, *i.e.* direct aging.[19,22] Recently, this treatment has received a lot of interest in the field of L-PBF, mostly regarding Al alloys.[25–28] One of its advantages consists in the exploiting of the supersaturated condition reached after the L-PBF process due to extremely high cooling rates (10^3 to 10^6 °C/s[7]). This also applies to NiTi parts, since supersaturation is necessary for the control of TTs through the precipitation reaction.[11] Direct aging also reduces the costs of L-PBF parts by avoiding solution annealing, which is a high temperature and energy-intensive step of the treatment. This makes the L-PBF route more attractive. In addition, for NiTi parts, solution annealing has been found challenging due to unwanted outcomes such as melting and oxidation.[19]

The present work aims at identifying the effects of different short-time direct aging heat treatments on the microstructure and superelastic properties of NiTi samples manufactured through L-PBF, with the aim of making this process route more appealing for the production of NiTi tailor-made biomedical components. Direct aged alloys were compared to the solution annealed and aged ones, analyzing the transformation temperatures (TTs), the microstructure and the superelastic behavior at room temperature and 37 °C. To provide a comprehensive characterization on the effects of aging without solution annealing, the direct aged samples were analyzed using transmission electron microscopy (TEM). Compression tests up to failure and Vickers microhardness tests were also performed to analyze more in-depth the material behavior.

II. MATERIALS AND METHODS

NiTi cylindrical samples (8 mm in diameter and 40 mm in height) were manufactured in the vertical direction starting from powder with 52.39Ni-47.61Ti nominal chemical composition (at pct) with the process parameters reported in Table I. A preliminary characterization aimed at determining the effects of the different sets of process parameters used was conducted in terms of microstructural characterization and microhardness tests. The results, not reported here for the sake of brevity, showed negligible differences between samples, *e.g.* the measured size of the chessboard macrostructure was between 68 and 70 μm, while the hardness scattering remains below 5 pct among all the samples, which throughout the test will be generically referred to as "as-built samples", disregarding the small differences in the process parameters.

A Nabertherm P330 furnace was used to carry out heat treatments. Aging heat treatments without prior solution annealing, *i.e.* direct aging, were performed. Two different temperatures were used for the aging step, 400 °C and 500 °C, for a short exposure time of 15 min followed by water quenching. For comparison, some samples were treated with solution annealing followed by aging. Solution annealing was performed at 950 °C for 5.5 h followed by water quenching. For the subsequent step, the same aging treatments described for the direct aging were used.

Details of the analyzed conditions are reported in Table II, where the solution annealed and aged samples are referred to as S 400 °C and S 500 °C, while the direct aged samples as DA 400 °C and DA 500 °C.

The TTs were measured using differential scanning calorimetry (DSC – Q100 – TA Instruments) analyses involving subsequent thermal cycle of heating and cooling between − 90 °C and 180 °C, with a heating/cooling rate of 10 °C/min.

Crystalline structures of the samples were determined by using a Panalytical X'Pert PRO diffractometer equipped with a X'Celerator detector (X-ray source: Cu Kα, λ = 0.154 nm; generator settings: 40 mA, 40 kV). XRD patterns were collected at room temperature in a 2θ range of 10° ÷ 100° (step Size: 0.0170° 2θ; scan step time: 30 s).

Microstructure was investigated through LEICA DMI 5000 M optical microscope and scanning electron microscope (SEM) Leo Evo 40XVP on samples obtained using Imptech Pc10 precision cutter, cold mounted and polished with silicon carbide abrasive papers up to mirror finishing. Chemical etching was performed for 150 to 200 s using 10 pct HF, 40 pct HNO_3 and 50 pct H_2O solution.

Porosities were characterized in terms of fraction of area, roundness and surface distribution through the analysis of eight optical microscopic images, each with an area of 0.6 mm^2. The fraction of porosities (pct) was determined as the ratio between the total area of porosities and the analyzed area of samples. The roundness was calculated through the following equation, according to the instrument guide:

$$R = \frac{2p}{4\pi A \times 1.064}$$

where R is the roundness, $2p$ and A are respectively the perimeter and area of the pore, and 1.064 is a corrector factor for the image digitalization.

Samples for compression tests were machined to final size of 4.5 mm in diameter (d) and 6.75 mm in length (l), to ensure a l/d of 1.5. Compression tests were performed along the building direction using a Instron mod. 3369 machine (load cell of 50 kN) with a strain rate of 10^{-3} s^{-1}, both at room temperature (RT) and at 37 °C. Experiments at RT were conducted in two different modes, *i.e.* cyclic loading-unloading up to 6 pct of

Table I. Process Parameters Used for NiTi Component Production *via* L-PBF

Laser Power (W)	Scan Speed (mm/s)	Hatch Spacing (μm)	Spot Size (μm)	Layer Thickness (μm)
150-180	500-1000	80	60	60

Table II. Investigated Conditions of the Present Work

Condition	Heat Treatment
As-built	—
S 400 °C	950 °C 5.5 h WQ + 400 °C 15 min WQ
S 500 °C	950 °C 5.5 h WQ + 500 °C 15 min WQ
DA 400 °C	400 °C 15 min WQ
DA 500 °C	500 °C 15 min WQ

deformation 15 times and incremental cyclic tests from 1 to 10 pct of deformation, and were repeated two times per condition. Compression tests at 37 °C were carried out in the cyclic mode. Compression tests were chosen for the characterization since most of the biomedical devices are compressed during exercise as well as during their delivery in the human body (*e.g.* vascular stents).

To provide a complete characterization of the DA samples, transmission electron microscopy (TEM) inspections were performed using a Philips™ CM20® microscope operating at 200 kV and equipped with a double tilt specimen holder and a liquid nitrogen cooling stage. Discs of 3 mm diameter were extracted from the AM cylindrical samples at the xy plane, using a precision cutting tool, and then ground to an average thickness of 100 μm. Double-side dimpling was carried out to a disc-center mean thickness of 30 μm. Final thinning to electron transparency was obtained by using a dual-beam Gatan™ PIPS.

Detected phases were identified using selected area electron diffraction (SAD). With this respect, R-phase was identified by diffraction spots occurring at $1/3 < 110 >$ positions in the $< 111 >$ -matrix SAD patterns. In this crystal orientation, the coherent Ni_4Ti_3 phase, whenever present, can be recognized by SAEDP additional diffraction spots at $1/7 < 123 >$ -matrix positions.

Statistic evaluations of mean size, distribution, and volume fraction of the Ni_4Ti_3 phase particles were carried out by orienting the foil normal to the $[1\bar{1}0]$ direction. Foil thickness, t_{TEM}, was measured by converged electron beam diffraction (CBED). This was performed by analyzing the corresponding diffracted beam intensity variation under dual beam conditions. Thence, linear interpolation of data points in a $S^2/n_{fringes}^2$ *vs* $n_{fringes}^{-2}$, where S is the fringes spacing, and $n_{fringes}$ the number of counted fringes, was used to determine t_{TEM}. Crystal thickness, t_{TEM}, was measured in the areas, A, from which particle measurements were carried out.

Particle size, d, was measured by stereographic methods according to EN-112 using an image analysis software (Image pro-plus®). Particle edge-to-edge spacing, λ, was determine by stereological method through $\lambda = (N/V)^{-1/3}$, being N the total number particles measured and $V = A{\cdot}t_{TEM}$ the total inspected TEM crystal volume from which the measurements were taken. Particle volume fraction, f_V, was determined by Woodhead method in which the volume number fraction is determined by $N_V = N_A/d$. For each size group, $N_A(i) = n_i/(A/M^2)$ represents the thin foil are fraction recorded by tilting the thin foil at $[111]_{B2}$, that is where the longest lenticular axis of the Ni_4Ti_3 phase particles are lying, where n_i are the number of particles in specific size groups, and A is the area from which particle sizes are measured and counted at magnification M. Thence, $N_V(i) = N_A(i)/(t_{TEM} + (i - 1/2)\Delta)$, being t_{TEM} the thin foil thickness measured in the area of acquisition and $(i - 1/2)\Delta$ is the mean diameter in the size group (i).

Using this stereological approach, the Ni_4Ti_3 particle volume fraction is calculated as follows:

$$f_V = \frac{\pi}{6}\Delta^3 \sum N_{V(i)}(i - 1/2)^3$$

and the related values were obtained by evaluating more than 2500 particles from several TEM disc areas and from three different TEM discs per experimental condition.

Vickers microhardness and compression tests up to failure at RT were also performed on the DA samples, with the aim of providing a deeper understanding of their mechanical behavior in relationship to the microstructure. Microhardness measurements were carried out on the xy plane for each sample with a Mitutoyo HM-200 hardness tester, using a load of 100 g applied for 15 s, for a total number of ten indentations.

III. RESULTS AND DISCUSSION

A. *Phase Transformation*

Figure 1 displays the DSC thermograms of virgin powder, as-built and heat-treated samples, and Table III shows the resulting TTs.

The DSC curve of the powder presents large and adjacent peaks during both the heating and cooling scan, due to the A ↔ M (B2 cubic ↔ monoclinic B19' lattice[29]) phase transformation occurring at multiples and continuous temperatures, as a result of the compositional heterogeneity of powder.[30] The as-built alloy exhibits only a single peak on both cooling and heating, which corresponds to the A → M direct transformation and M → A reverse transformation, respectively. It should be noted that the leftmost peak detected in the cooling scans of powder and as-built sample is not completely observable, due to the limited examined temperature range. These peaks are associated to the

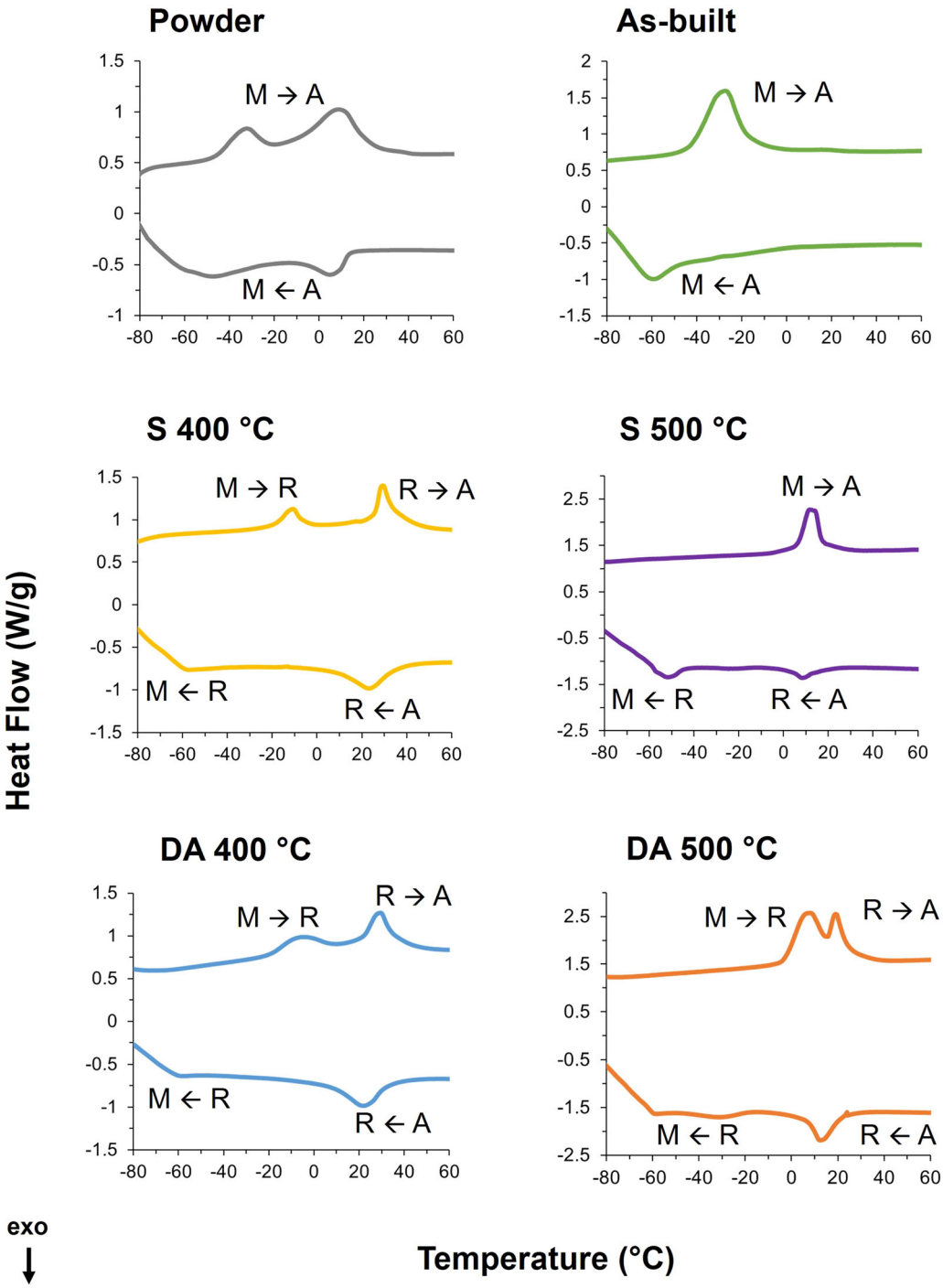

Fig. 1—DSC thermograms for powder, as-built and heat-treated samples.

A → M transformation, which in these cases did not complete in the examined range and therefore M_f could not be accurately determined due to the instrument limits. Both the powder and the as-built sample are characterized by an A_f lower than room temperature, thus denoting the presence of the austenitic phase at room temperature.

TTs were also determined for the as-built sample after solution annealing to estimate the chemical composition of the alloy after L-PBF process. The results, not reported here for the sake of brevity, showed a M_s temperature of − 9 °C, which, compared to the literature,[31,32] suggests a Ni content (at pct) approximately between 50.5 pct and 51 pct, pointing out that more than 1 pct of Ni evaporated during the process.

The double peaks observed in the DSC scans for all the heat-treated alloys suggest the presence of the R-phase (R). This is an intermediate phase appearing sometimes in the transformation of austenite into martensite, resulting from the trigonal distortion of the

Table III. Transformation Temperatures of Powder, As-Built and Heat-Treated Samples

	Temperature (°C)								
Material	M_f	M_p	M_s	R_f	R_p	R_s	A_s	A_p	A_f
Powder	< − 70	− 48	− 14	—	—	—	− 48	8	23
As-built	< − 70	− 60	− 31	—	—	—	− 43	− 27	− 16
S 400 °C	< − 70	− 58	− 40	9	23	36	25	29	35
S 500 °C	< − 70	− 57	− 42	2	8	16	6	12	17
DA 400 °C	< − 70	− 60	− 44	4	22	33	21	29	37
DA 500 °C	− 46	− 31	− 19	6	12	22	16	19	25

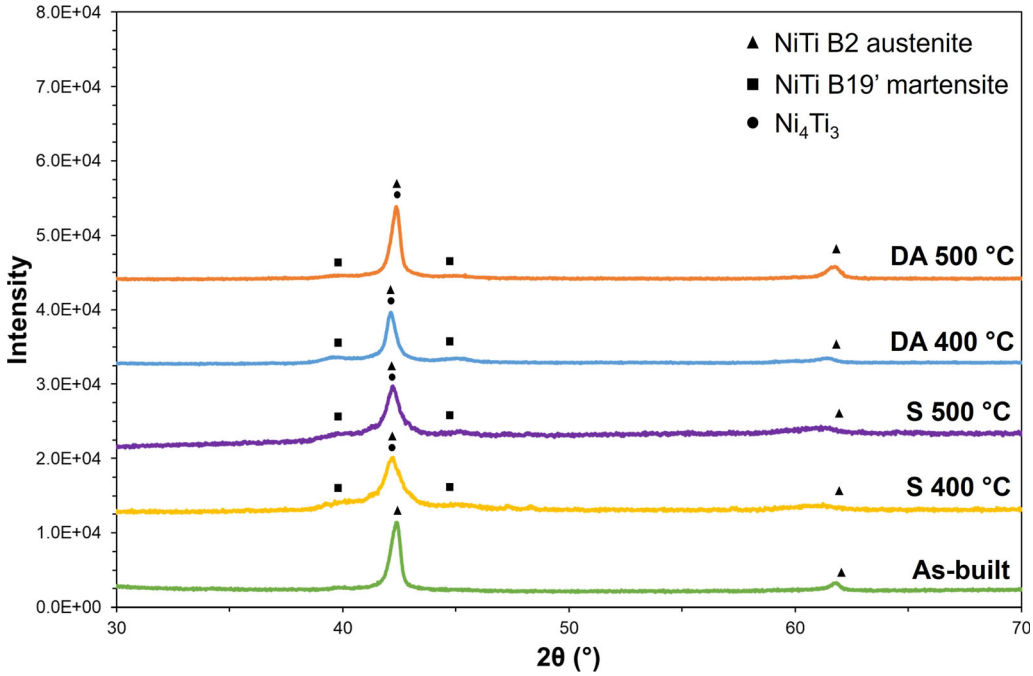

Fig. 2—XRD spectra of the as-built, S 400 °C, S 500 °C, DA 400 °C and DA 500 °C samples.

B2 structure. The R-phase transformation can be classified as symmetric ($A \rightarrow R \rightarrow M$ on cooling, $M \rightarrow R \rightarrow A$ on heating) for S 400 °C, DA 400 °C and DA 500 °C samples, while asymmetric ($A \rightarrow R \rightarrow M$ on cooling, $M \rightarrow A$ on heating) for S 500 °C.[33] The second cooling peak ($R \rightarrow M$) is not evident for S 400 °C, DA 400 °C and DA 500 °C. However, the two-step transformation during heating and the very small temperature hysteresis between the austenite peak and the R-phase peak ($|A_p - R_p| < 10$ °C) allow the identification of the R-phase. In fact, the $A \leftrightarrow R$ transformation is characterized by a very small temperature hysteresis compared to the $A \leftrightarrow M$ transformation.[33] Since the $R \rightarrow M$ transformation is not completely observable for S 400 °C, DA 400 °C and DA 500 °C, the relative M_f temperature was not accurately determinable due to the instrument limits.

R-phase is connected to the presence of Ni_4Ti_3 precipitates, which are known to form after solution annealing and aging between 400 and 600 °C in the conventionally manufactured NiTi components.[9,11] The presence of these particles, if nano-sized and placed at small relative distances, generates strain fields able to promote $A \rightarrow R$ transformation over $A \rightarrow M$. This is due to the smaller transformation strain involved by the R-phase compared to martensite if precipitates are present.[32,34] The increase of the TTs in the heat-treated alloys compared to the as-built also confirms the presence of Ni_4Ti_3, as their formation involves a decrease in the Ni content of the matrix. It is in fact well established that the increase of the TTs is associated to the loss of Ni content in the matrix, which can originate by the formation of Ni-rich secondary phases during heat treatment or by the Ni evaporation during the process.[8,11,35–37]

By comparing the samples aged at the same temperature, with and without solution annealing, it appears that the TTs are almost superimposable, especially for S 400 °C and DA 400 °C. The small variation observed between S 500 °C and DA 500 °C is mainly attributed to

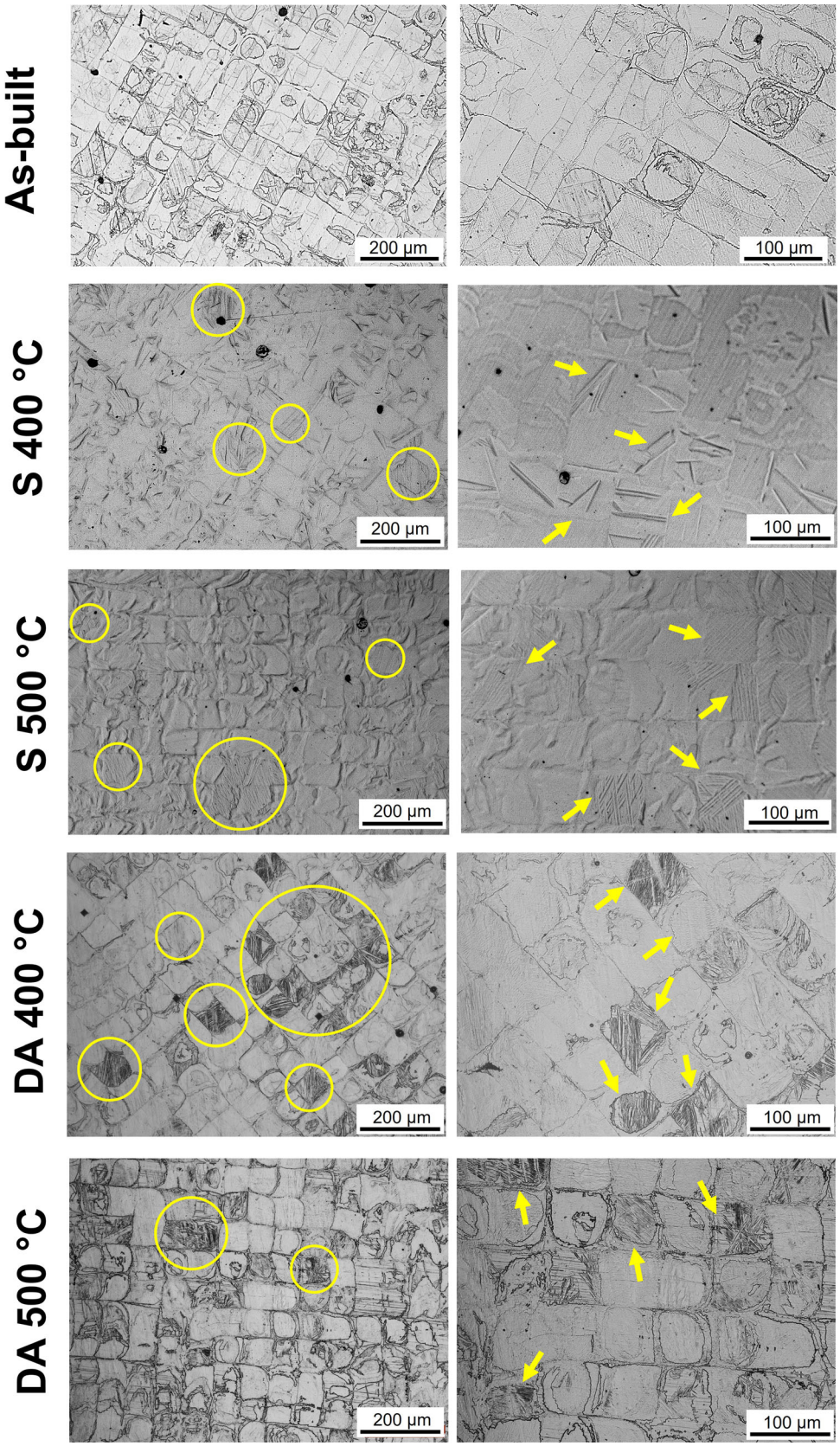

Fig. 3—Micrographs of as-built cylinders, as well as the S 400 °C, S 500 °C, DA 400 °C and DA 500 °C.

the asymmetric nature of the R transformation recorded for S 500 °C. However, the austenite TTs, which determine the superelastic behavior, appears similar also between S 500 °C and DA 500 °C. This denotes that the effect of solution annealing on TTs is negligible compared to the effect of the aging for the purpose of obtaining TTs suitable for the superelasticity.

B. *Phase Analysis and Microstructure*

Figure 2 displays the XRD spectra of the specimens. According to the literature, all samples show the principal peaks of B2 austenite.[38,39] In the case of the heat-treated alloys, B19' martensite can also be detected,[39,40] which is attributable to residual martensite due to the non-completed M → A transformation at room temperature. This agrees with the DSC analysis (Figure 1). The peaks related to Ni_4Ti_3 overlap with those of B2 phase,[30,41–44] therefore it is not easy to clearly identify their presence. However, based on the literature, the formation of Ni_4Ti_3 can be reasonably assumed for the heat-treated samples. This is further confirmed by the DSC scans, which show the presence of the R-phase and the increase of TTs after the heat treatments (Figure 1).

Micrographs along the xy plane at are reported in Figure 3 for all the investigated conditions. The observable macrostructure has a chessboard shape, which reflects the alternating laser scanning path used during production.[20,45] Similar textures have already been detected in L-PBF NiTi.[46–51] The substructures (''islands'') observable within the chessboard texture are characterized by squared shape. The main influence on their shape is generally attributed to the hatch spacing parameter, whose variation leads to changes from squared to polygonal or irregular shape.[49–51]

The chessboard texture in the as-built alloy is characterized by a width of the substructures of 70 ± 6 μm, which is slightly smaller than the hatch spacing, *i.e.* 80 μm. This can be attributed to a smaller spot size relative to the hatch spacing and denotes that no scan overlap occurred.[9]

The chessboard structure was maintained after all the heat treatments performed. The width of the islands was found to be 70 ± 4 μm for S 400 °C, 70 ± 3 μm for S 500 °C, 70 ± 5 μm for DA 400 °C and 71 ± 4 μm for DA 500 °C, thus pointing out that no significant modifications in the chessboard texture took place after heat treatments.

Within the chessboard pattern of the as-built alloy, only ''smooth'' squares are observed, with no martensitic structures. In fact, according to the XRD and DSC analyses, this sample only present the B2 austenite phase at room temperature. On the other hand, all the heat-treated samples show some martensitic structures inside the chessboard pattern, pointed out by the yellow circles and arrows. These, according to the XRD analysis, can be identified as the B19' martensitic phase. Ni_4Ti_3 precipitates are not observable at these magnifications for either solution annealed or direct aged alloys due to their nanometric dimensions.

From the comparison of the direct aged specimens, it appears that martensite is more evident in the DA 400 °C sample compared to the DA 500 °C. This is due to the different A_f temperatures (37 °C and 25 °C, respectively), which point out that especially for DA 400 °C sample the transformation is still occurring at room temperature and thus more martensite is present in this case.

Details of an island of the chessboard texture and martensite structures at higher magnification are provided in Figure 4 for some of the analyzed conditions, for illustrative purposes.

Figure 5 reports the results of the SEM analyses, which reveal the same macrostructures identified through the optical microscope, *i.e.* squared shape chessboard texture for all the conditions and the presence of the martensitic phase in the heat-treated ones.

Results of the porosity analysis for the as-built, S 400 °C, S 500 °C, DA 400 °C and DA 500 °C conditions are reported in Figure 6. A very low porosity fraction can be observed for the as-built alloy, which remains negligible after the direct aging heat treatments, while increases after solution annealing and aging. This is due to the high temperature of the solution annealing treatment, which promotes the growth of the existing gas pores, resulting in the rise of the fraction of area of porosities. The analysis of the surface distribution showed that most of the porosities present an area lower than 50 μm^2. Furthermore, the roundness of pores was found to be close to 1 for each of the analyzed samples, denoting their spheric morphology. This demonstrates that most of the generated pores are mainly due to the absorption of the gas surrounding the material during the L-PBF process rather than lack of fusion defects.[7,52]

C. *Stress–Strain Response at RT*

1. *Cyclic compression tests*

Stress-strain curves obtained from cyclic compression tests at RT for the as-built and heat-treated samples are reported in Figure 7, where solution annealed and direct aged samples are grouped by the aging temperature for a better comparison. Each specimen underwent 15 cycles of loading up to 6 pct strain, commonly considered as the limit for superelasticity, and unloading to 0 pct.

A pseudoelastic behavior can be observed in each condition (Figure 7), with the formation of stress-induced martensite from the austenitic phase during the application of load, pointed out by the flattening of the curve, which is commonly shown also during both tension and torsion tests.[53] This part of the curve is commonly referred to as ''Luders-like'' deformation and is associated with martensite reorientation and detwinning processes.[54,55] Stress-strain behavior is almost superimposable for the heat treatments carried out at the same temperature (*i.e.* aging), thus pointing out the minor effects of the presence of the solution annealing step compared to the aging temperature.

For every cycle, the maximum stress (σ_{MAX}), the pseudoelastic stress (σ_{PE}), *i.e.* the critical stress to induce

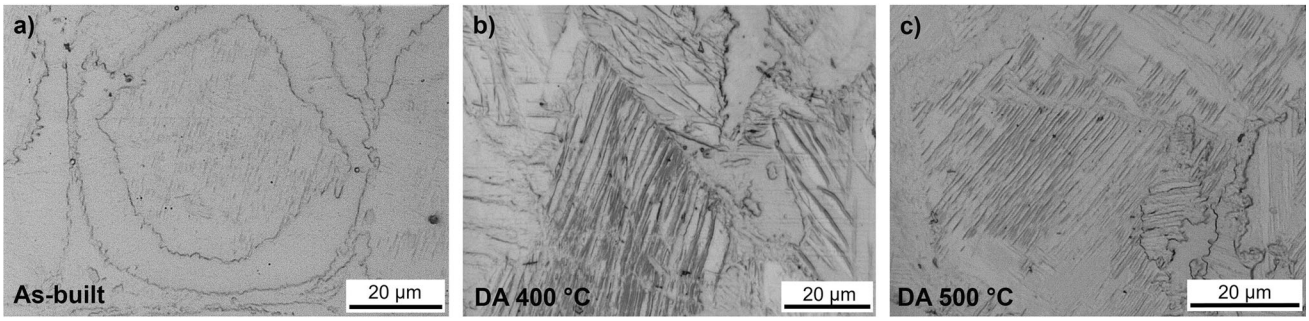

Fig. 4—Microstructural details of a chessboard substructure (*a*), and martensitic structures (*b*, *c*).

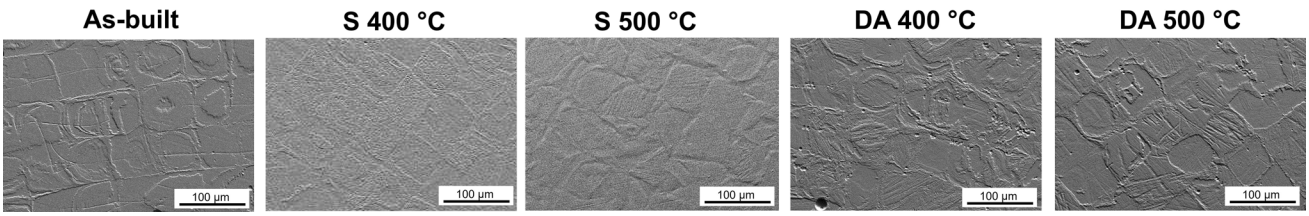

Fig. 5—SEM images of as-built cylinders, as well as S 400 °C, S 500 °C, DA 400 °C and DA 500 °C.

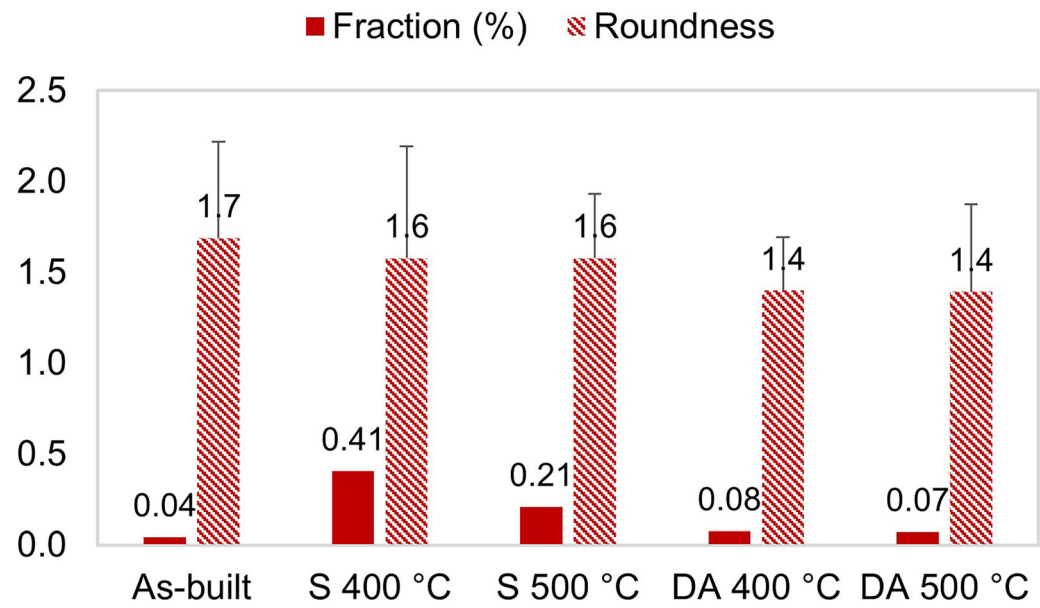

Fig. 6—Fraction of area and roundness of the porosities for as-built and heat-treated cylinders.

the martensitic transformation, and the residual strain associated to each cycle (ε_{RES}) were determined, and the results are summarized in Figure 8. σ_{PE} was graphically determined at the inflection point using the tangent method where it was visually identifiable.

By analyzing σ_{MAX} and σ_{PE} (Figures 8a, b), it emerges that higher values are reached by the as-built alloy, followed by S 400 °C and DA 400 °C and then by S 500 °C and DA 500 °C. The σ_{MAX} and σ_{PE} of the heat treatments performed at the same temperature are almost equal one to each other, reflecting what seen in Figure 7.

During the first cycles, the as-built specimen shows an increasing trend for σ_{MAX}, which then stabilizes at about 700 MPa from cycle 6, while a lower σ_{PE} value is recorded only in the first cycle due to the marked difference in the shape of the first curve (Figure 7). It should be noted that σ_{PE} could not be determined for cycles from 12 to 15 for the as-built condition, due to the gradual disappearence of the inflection point in the curves, pointing out an instability of the pseudoelastic behavior as the number of cycle increases.

On the other hand, all the heat-treated alloys show a lower σ_{MAX} value in cycle 1 (S 400 °C 555 ± 1 MPa, DA 400 °C 542 ± 15 MPa and S 500 °C

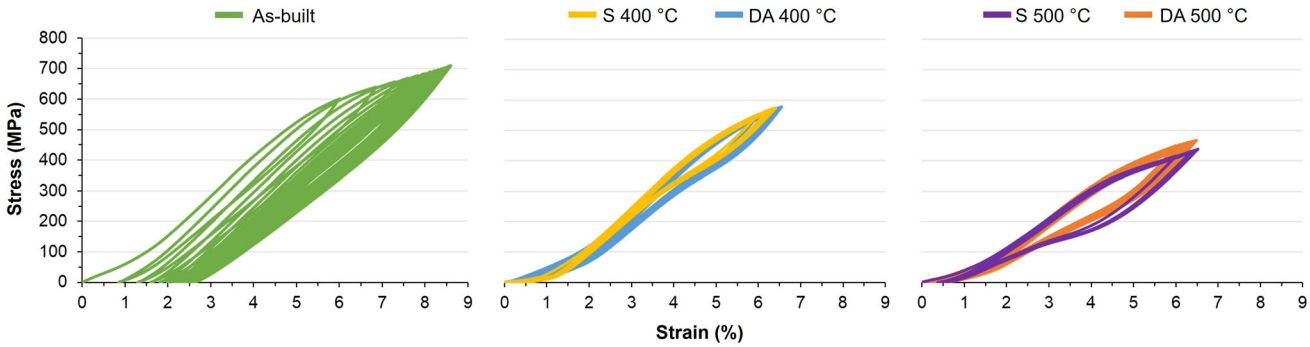

Fig. 7—Stress-strain responses of as-built and heat-treated samples tested under cyclic tests at RT.

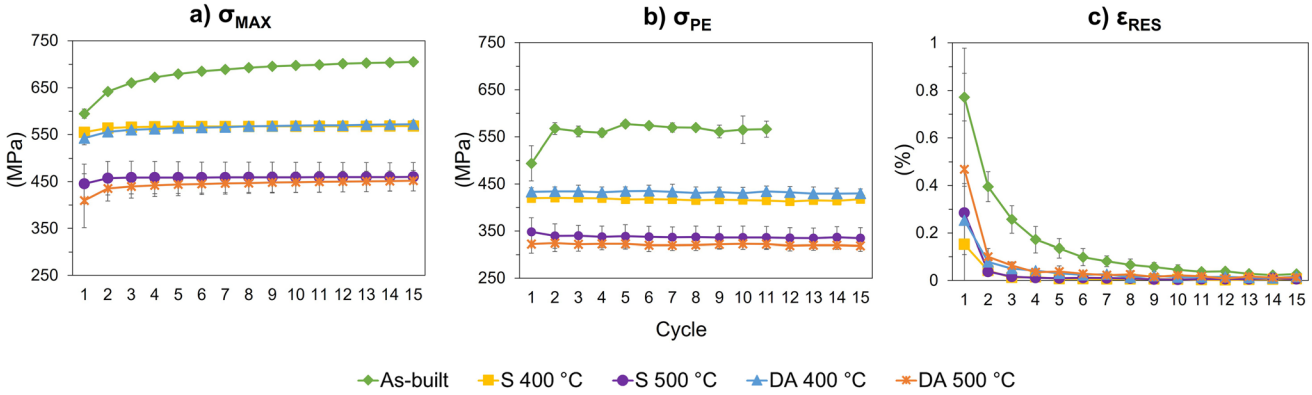

Fig. 8—Results of cyclic compression tests at RT: (*a*) maximum stress, (*b*) pseudoelastic stress and (*c*) residual strain as function of each cycle.

445 ± 42 MPa, DA 500 °C 409 ± 58 MPa), which then increases and remains constant from cycle 2 (around 570 MPa for both S 400 °C and DA 400 °C, and 450 MPa for both S 500 °C and DA 500 °C). Thus, for all the heat-treated samples σ_{MAX} settles after cycle 1, while σ_{PE} is stable from the first cycle. This denotes an overall greater stability in the stress-strain responses for the heat-treated conditions compared to the as-built. For each sample, a difference between σ_{MAX} and σ_{PE} in the range 120-150 MPa is recorded, considered after stabilization.

All the heat-treated samples show lower values of σ_{PE} compared to the as-built (Figure 8b). In detail, heat treatments at 400 °C lowered σ_{PE} by approximately 135 MPa, while heat treatments at 500 °C by about 240 MPa compared to the as-built condition. This because after aging austenite easily transforms into martensite due to the presence of local stress intensification field around Ni-rich precipitates, thus acting as nucleation sites for the transformation.[56,57] Lower σ_{PE} values can be also associated to the increase of TTs respect to the as-built alloy,[18,22] which agrees with the DSC results (Table III).

By comparing the σ_{MAX} values of the as-built and heat-treated alloys (Figure 8a), it appears that lower values are reached by the heat-treated ones. This points out that up to 6 pct of deformation the performed heat treatments enhanced the superelastic properties in compression by lowering σ_{PE} rather than increasing the maximum stress reached at 6 pct of strain.

Concerning ε_{RES} (Figure 8c), the as-built sample exhibits the highest values, denoting poor superelastic features. In this case dislocations formed during deformation, generating plasticity as well as stabilizing some martensite variants during loading, which inhibits the reverse transformation upon unloading and the consequent total recovery of the deformation.[17] On the contrary, all the heat-treated conditions present comparable negligible values of irreversible strain (lower than 0.1 pct for each cycle after stabilization, which occurred after the first cycle).

The total accumulated strain after 15 cycles at 6 pct of deformation is 2.2 ± 0.5 pct for the as-built sample, 0.3 ± 0.2 pct for S 400 °C, 0.4 ± 0.1 pct for S 500 °C, 0.6 ± 0.1 pct for DA 400 °C and 0.9 ± 0.6 pct for DA 500 °C, confirming the higher superelasticity of the heat-treated alloys.

The remarkable superelastic features obtained after the performed heat treatments are attributed to the presence of the Ni_4Ti_3 precipitates resulting from aging. The latter favor the superelastic features of the alloy by raising the stress required for slip plastic deformation. In this way, the achievement of the critical stress to induce the martensitic transformation (σ_{PE}) is eased, since from a thermodynamic point of view it is easier to form martensite when the stress is applied rather than causing plastic deformation. The formation of stress-induced martensite is therefore favored before the occurrence of slip.[58–60] Furthermore, Ni_4Ti_3 precipitates are known

to act as nucleation sites for the formation of martensite, thus promoting the martensitic transformation.[17,22,57]

2. *Incremental compression tests*

The effect of incremental cyclic loading (from 1 to 10 pct of strain) at RT was also investigated and the stress-strain curves for each condition are reported in Figure 9. The general trend previously observed for cyclic tests is confirmed, with an overall pseudoelastic behavior emerging from each condition. Improved superelastic features are evident for the heat-treated alloys, which show a similar behavior by comparing the conditions at the same aging temperature. Also, similarly to the cyclic tests, the lowering of the curves is detected as the aging temperature increases, as well as a greater definition of the pseudoelastic behavior.

Results of σ_{MAX}, σ_{PE} and ε_{RES} are reported in Figure 10 as function as the number of cycles, which in this case corresponds to the applied strain.

The σ_{MAX} and σ_{PE} (Figures 10a, b) for samples aged at the same temperature, with and without solution annealing, are nearly identical to one another, as previously detected in the cyclic tests.

As expected, σ_{MAX} raises as the number of cycles increases, as each cycle corresponds to an increase of the applied deformation (Figure 10a). The as-built specimen reaches higher σ_{MAX} compared to heat-treated samples from cycle 4 to 9, while results are almost superimposed for the other cycles.

For each condition, σ_{PE} was not clearly identifiable in the early cycles, where in fact samples present a linear behavior due to the very low strains involved, and consequently it could not be determined (Figure 10b). In

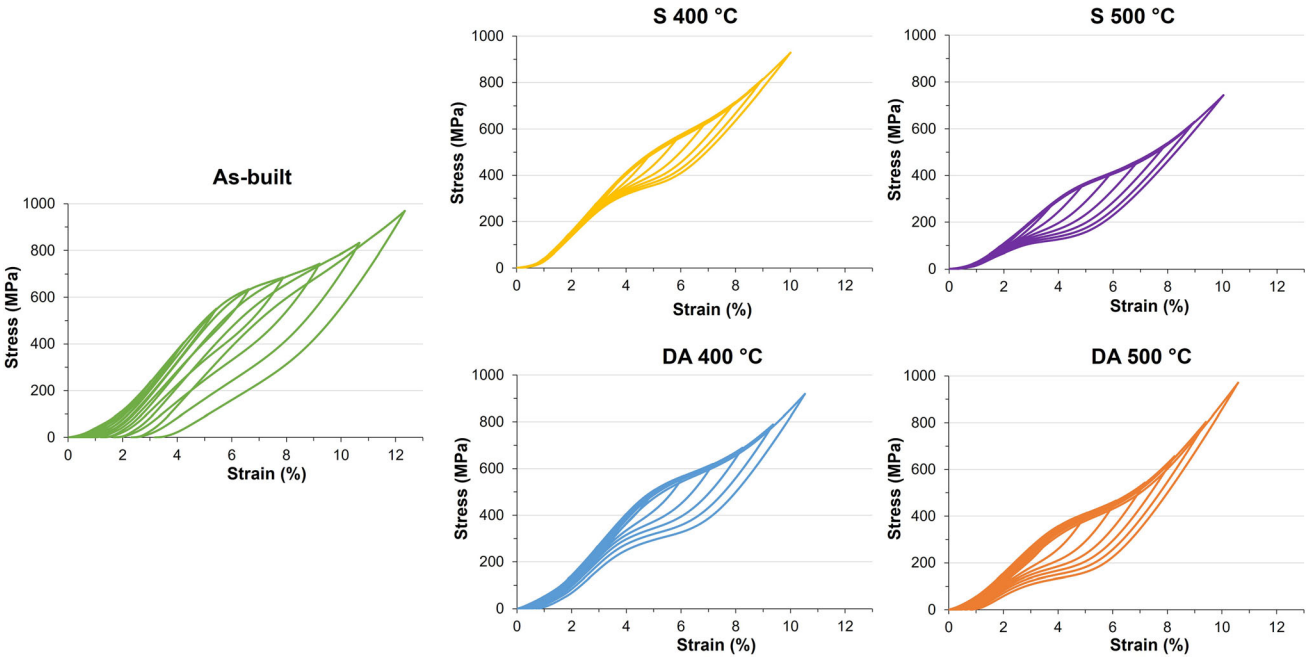

Fig. 9—Stress-strain responses tested under incremental tests at RT for as-built and heat-treated samples.

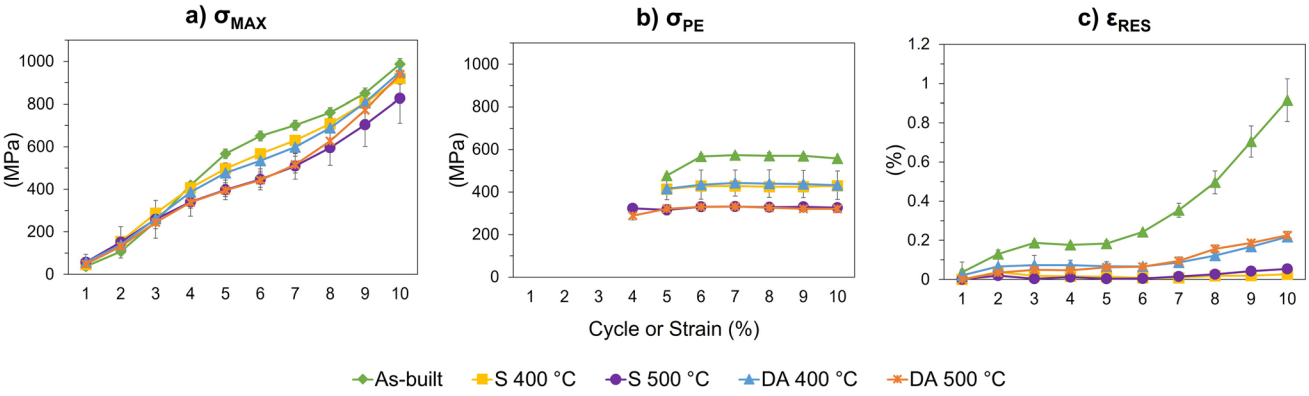

Fig. 10—Results of incremental compression tests at RT: (*a*) maximum stress, (*b*) pseudoelastic stress and (*c*) residual strain as function of each cycle.

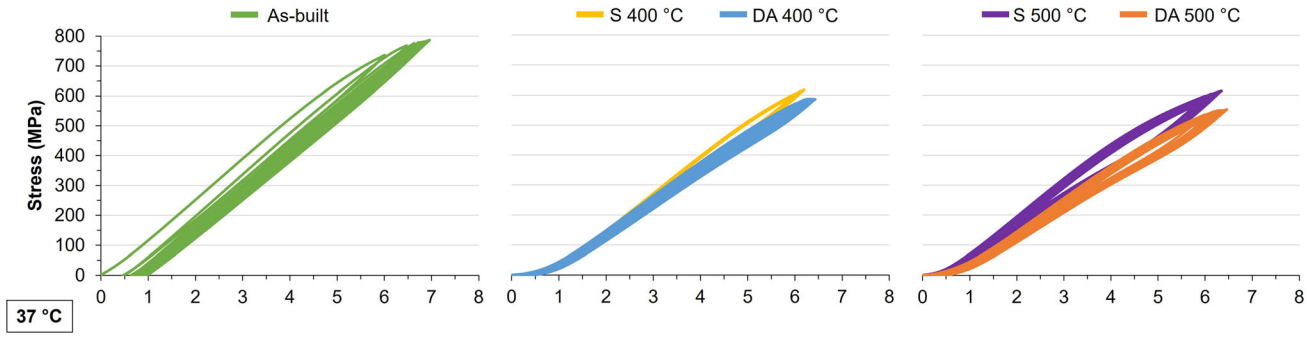

Fig. 11—Stress-strain responses of as-built and heat-treated samples tested under cyclic tests at 37 °C.

Table IV. Residual Deformation for All Samples Tested at 37 °C

	$\varepsilon_{RES,TOT,37\ °C}$ (Pct)
As-built	0.90 ± 0.09
S 400 °C	0.18 ± 0.02
S 500 °C	0.35 ± 0.01
DA 400 °C	0.44 ± 0.01
DA 500 °C	0.48 ± 0.02

this regard, it should be noted that both S 500 °C and DA 500 °C exhibits pseudoelastic behavior starting from 4 pct, while others from 5 pct. Values of σ_{PE} are higher in the as-built alloy, followed by S 400 °C and DA 400 °C and then by S 500 °C and DA 500 °C, confirming the general trend observed during cyclic compression tests. For each condition, σ_{PE} does not vary as the applied deformation increases, which is in agreement to what observed during incremental compressive tests by Saedi *et al.*[19] σ_{PE} stabilizes at values around 570 MPa for the as-built sample, 430 MPa for both S 400 °C and DA 400 °C and 320 MPa for both S 500 °C and DA 500 °C. Heat treatments at 400 and 500 °C lowers σ_{PE} of about 135 and 240 MPa compared to the as-built condition, which agrees to what found during cyclic compressive tests.

At equal applied deformation, ε_{RES} appears higher for the as-built, reaching 0.9 ± 0.1 pct in cycle 10, while both heat-treated specimens remain at values lower than 0.2 pct for each cycle, denoting a negligible irrecoverable strain (Figure 10c).

The total cumulative strain after 10 cycles of incremental deformation is 3.4 ± 0.3 pct for the as-built alloy, 0.2 ± 0.1 pct for S 400 °C, 0.2 ± 0.1 pct for S 500 °C, 1.0 ± 0.2 pct for DA 400 °C and 0.9 ± 0.1 pct for DA 500 °C, thus indicating the improvement of the superelastic behavior thanks to heat treatments. Therefore, it can be stated that superelasticity is achieved up to 10 pct of strain after all the heat treatments. This value is higher than both the limit of superelasticity, commonly identified as 6 pct, and what found in previous studies on additively manufactured components.[17–19,22]

D. *Stress–Strain Response at 37 °C*

Cyclic compression tests were repeated at the body temperature (37 °C) to investigate the feasibility of achieving superelasticity for possible biomedical applications. The corresponding stress-strain curves are displayed in Figure 11, while Table IV summarizes the total accumulated residual strain at 37 °C ($\varepsilon_{RES,TOT,37\ °C}$) at the end of the 15 cycles for each condition as the main result of the test.

Similarly to what previously observed in RT tests, the as-built alloy shows higher stress at equal strain compared to the heat-treated. The comparison among samples aged at the same temperature shows that solution annealed and aged samples reach slightly higher stresses compared to the direct aged ones.

The as-built alloy is characterized by poor superelastic features, while all the heat-treated alloys show higher stability of the superelastic effect (Figure 11), as well as negligible $\varepsilon_{RES,TOT,37\ °C}$ (Table IV). This is analogous to what previously found at RT due to the non-significant microstructural differences experienced at 37 °C by the alloys. In fact, Ni_4Ti_3 precipitates are preserved at 37 °C, and their size and distribution are not expected to change. Furthermore, according to the TTs (Table III), no substantial variations are expected at 37 °C in the matrices of the analyzed alloys. At this temperature both S 400 °C and DA 400 °C should again present austenite and martensite, while in both S 500 °C and DA 500 °C the austenite should be the solely phase present, and this is expected to further enhance the superelastic effect. Thence, heat treatments with aging at 500 °C appears to be preferable to those with aging at 400 °C in the perspective of biomedical applications. This is also confirmed by the more pronounced pseudoelastic behavior observed in Figure 11.

Each of the curves obtained at 37 °C shows slightly higher levels of stress reached (σ_{MAX} and σ_{PE}) compared to those at RT (compare Figures 11 through 7). This is due to the higher stability of the austenitic phase as the temperature rises, which leads to the need of greater stress for triggering the stress-induced martensitic transformation.[61] This is especially true for samples treated at 500 °C, *i.e.* S 500 °C and DA 500 °C, which at 37 °C are likely fully formed by austenite, rather than a mixed austenite-martensite structure as occurs at RT (A_f is of 17 °C and 25 °C, respectively).

The direct aged samples produced the same overall behavior compared to the solution annealed and aged ones, making the solution step unnecessary for the purposes of the superelasticity obtainment. This, together with the negligible residual strain observed both at RT and 37 °C, proves the effectiveness of short-time direct aging heat treatments on the superelasticity of NiTi parts produced through L-PBF. To better characterize the microstructural features responsible for the observed mechanical response for direct aged samples, TEM analysis was carried out on DA 400 °C and DA 500 °C samples.

E. *Direct Aging Characterization*

1. *Precipitates analysis*

Figure 12 displays representative TEM micrographs showing B2 austenite and B19' martensite phases in the direct aged samples, that is DA 400 °C (Figures 12a, b) and DA 500 °C (Figures 12c, d). B2 austenite grained structure in both conditions is characterized by high density of tangled dislocations. In fact, Figure 13 shows the typical dislocation morphology observed in the two direct aging conditions. DA 500 °C alloy tends to show a slightly higher tangled dislocation density compared to DA 400 °C. The austenite mean grain size is 1.2 μm and 0.9 μm after direct aging at 400 °C and after 500 °C, respectively (Figure 12). B19' martensite is shown in Figure 14 for both the direct aged samples. It was found that the volume fraction of B19' martensite in DA 400 °C sample was up to 50 pct more compared to the amount of it found in DA 500 °C. In addition, the R-phase was detected for each condition, and was observed at the B19' martensite lath edges, as reported in Figures 14 and 15. A greater amount of R-phase was found in DA 500 °C specimen.

In the B2 austenite grains several nanometric spheroidal oxide particles were found in both the DA samples, these are identified as Ni_4Ti_3O oxides. Yet, their size and distribution did not appear to be affected by the aging temperature (Figure 16).

One of the marked microstructure aspects that differentiate the two direct aging conditions is the presence and distribution of nanometric Ni_4Ti_3 phase

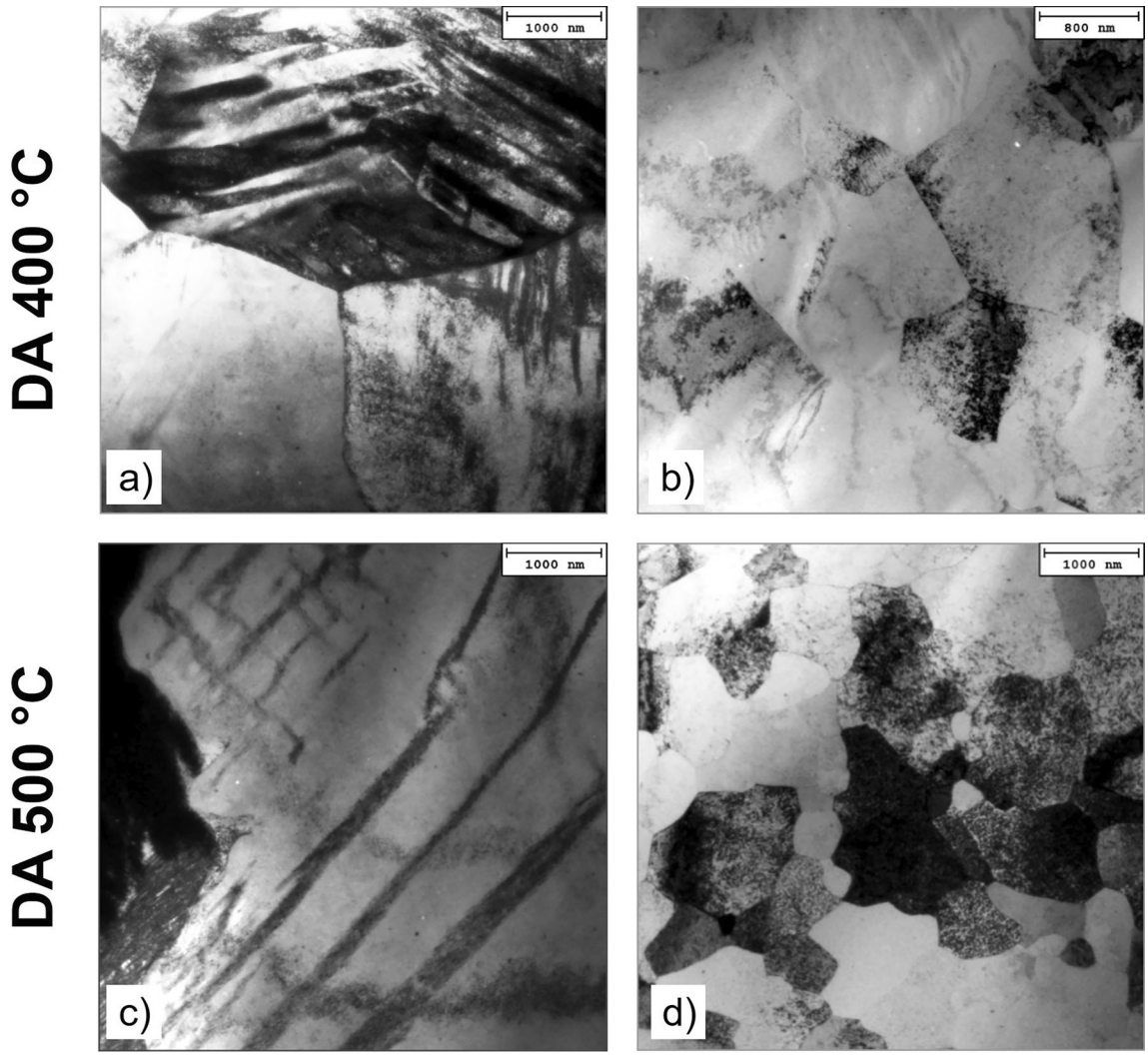

Fig. 12—LM of: (*a*, *b*) DA 400 °C, (*c*, *d*) DA 500 °C.

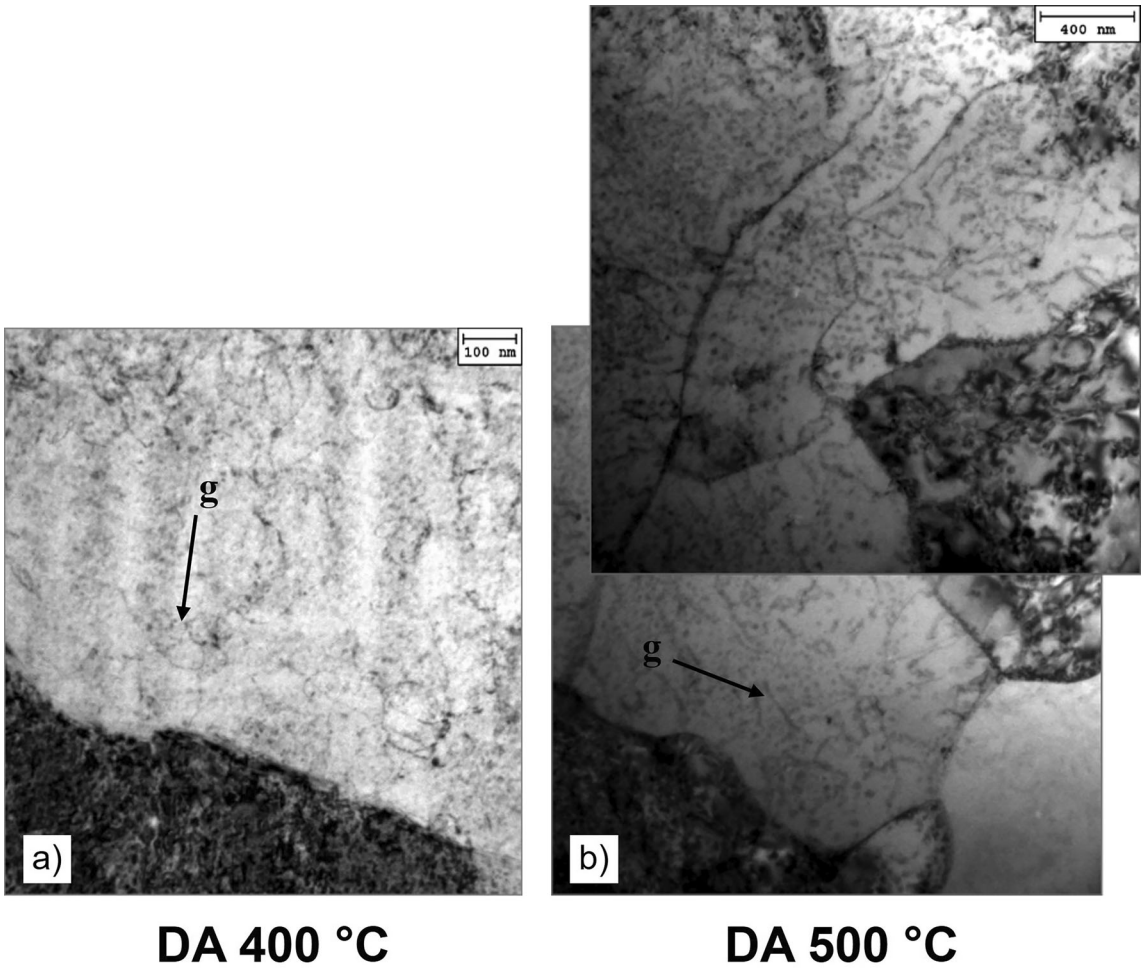

Fig. 13—TEM-BF showing dislocation network obtained under $[110]_{B2}$ g-vector in (*a*) DA 400 °C sample, (*b*) DA 500 °C.

precipitates. Figure 17 shows the typical distribution of these particles in the two direct aged alloys. It appears that volume fraction and quantity of Ni_4Ti_3 particles were significantly higher after direct aging at 500 °C compared to the 400 °C condition. In the DA 400 °C sample, the size distribution of the Ni_4Ti_3 precipitates tends to be uniform, with minimum-to-maximum sizes of ~ 8-to-60 nm. On the other hand, in the DA 500 °C sample, the Ni_4Ti_3 precipitates appeared to be less homogeneous, with minimum-to-maximum sizes of ~ 5-to-80 nm.

Histogram and statistic data reported in Figure 18 show that formation of Ni_4Ti_3 particles after direct aging at 500 °C is largely promoted accounting to 4-times higher volume fraction compared to the alloy direct aged at 400 °C for the same duration. At the same time particle spacing reduced to almost half from DA 500 °C with respect to DA 400 °C, being the mean size unaltered. TEM inspections showed that the higher presence of the Ni_4Ti_3 particles after direct aging at 500 °C is rather inhomogeneous throughout the material microstructure. In fact, these particles were found to preferentially precipitate within the B2 austenite grains and at their grain boundaries.

Ni_4Ti_3 is a metastable phase that is known to precipitate in NiTi shape memory alloy below 700 °C. Ni_4Ti_3 phase has a R3-space group with a rhombohedral unit cell structure (in which six Ti atoms alternate to eight Ni atoms[62,63]). The Ni_4Ti_3 particles habit plane is along $[111]_{B2}$ austenite matrix, with a total of eight variants.[62,63]

Ni_4Ti_3 phase typically has an orientation relationship to B2 matrix as $[121]_{B2} \parallel [1102]_{Ni4Ti3}$ and $[112]_{B2} \parallel [1102]_{Ni4Ti3}$.[62] Moreover, Ni_4Ti_3 phase and B2 austenite phase reflections overlap in the $[011]_{B2}$ and $[001]_{B2}$ orientations (see also[64]).

It was reported that Ni_4Ti_3 particles with size below ~ 100 nm generate coherency and semi-coherency with the B2 austenite matrix.[65–67] Ni_4Ti_3 precipitates have lenticular shape with lateral spacing increasing with aging time.[68]

On cooling from high temperatures, the B2 austenite phase can directly transform into the B19' martensite phase. On the other hand, the presence of Ni_4Ti_3 precipitates promotes the B2 to R-phase transformation,[68] as also reported in Figure 15. Thence, the presence of the Ni_4Ti_3 phase is likely to inhibit and eventually suppress the occurrence of martensitic

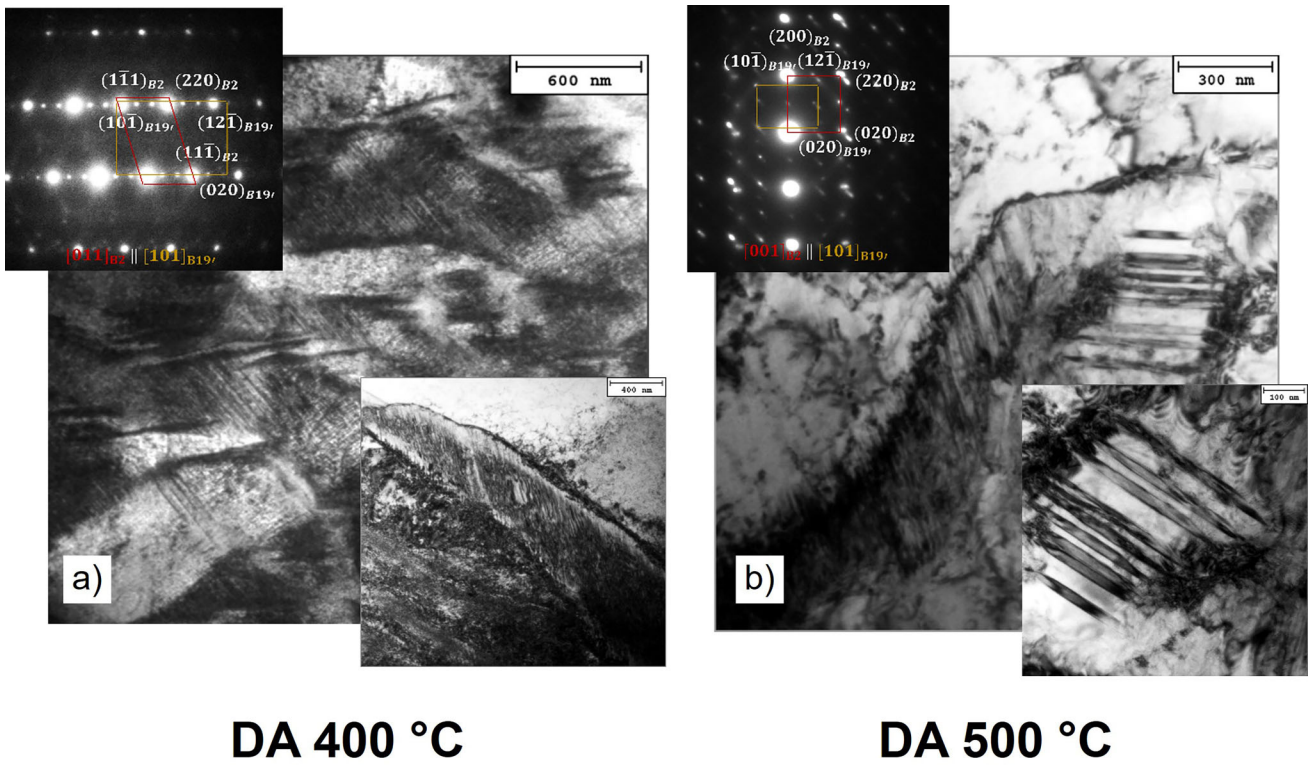

Fig. 14—B19' martensite phase in (*a*) DA 400 °C, (*b*) DA 500 °C.

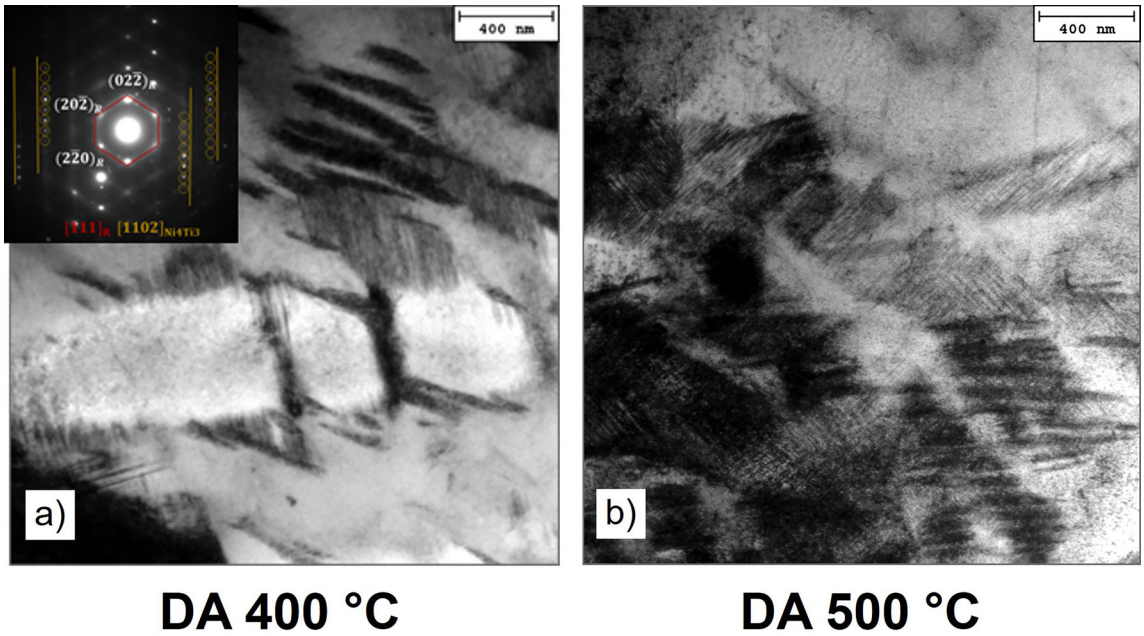

Fig. 15—Smooth constrained growth of R-phase induced by the presence of Ni_4Ti_3 precipitates. The micrographs document (*a*) the occurrence of early stages of R-phase formation in DA 400 °C sample, and (*b*) its evolution in DA 500 °C sample.

transformation, thus promoting formation of R-phase. That is, the occurrence of two-stage phase transformation of B2-R-B19' is mainly driven by the formation of Ni_4Ti_3 phase. In general, the R-phase nucleates at the interface between Ni_4Ti_3 phase and B2 austenite matrix, as well as B19' martensite nucleates at the interface between Ni_4Ti_3 phase and R-phase.[69,70]

The intermediate R-phase has a trigonal crystal structure.[69] This phase can be recognized by SAEDP as superlattice reflections are located at 1/3 positions

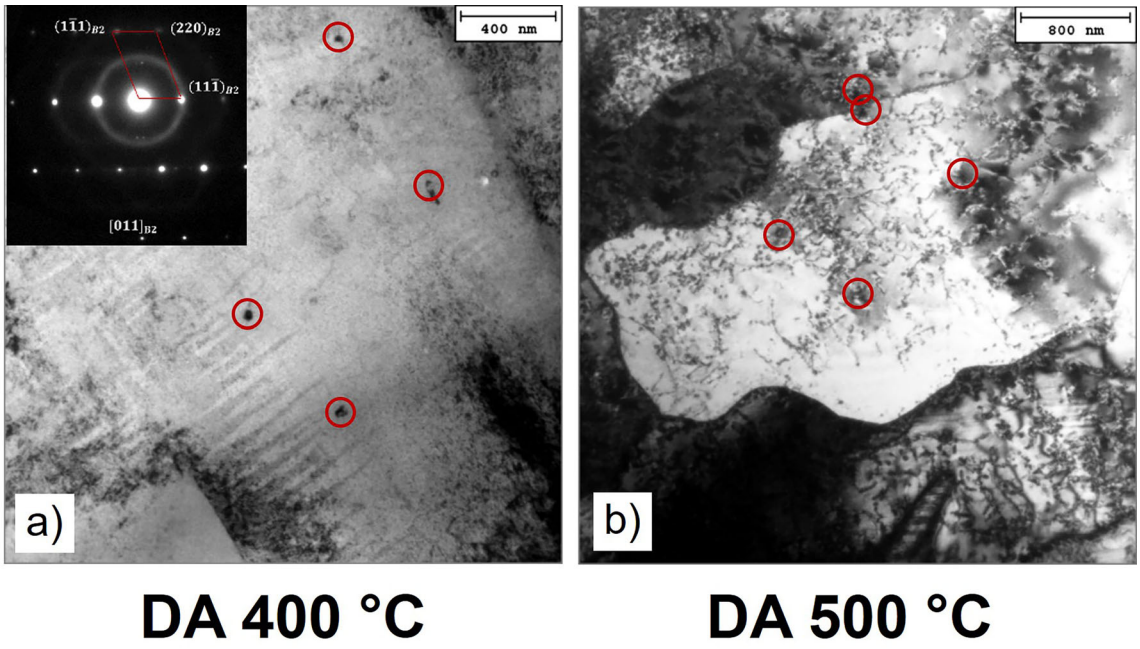

Fig. 16—Typical nanometer Ni_4Ti_3O oxide particles detected in (*a*) DA 400 °C, (*b*) DA 500 °C.

along $[110]_{B2}$ and $[111]_{B2}$ austenite matrix directions, in addition, $[111]_{B2} \parallel [111]_R$ variants can also be considered for the R-phase identification.

The existing supersaturation of Ni atoms within the B2 matrix promotes the homogeneous nucleation of the Ni_4Ti_3 precipitates, at first stages of aging, and the particle growth, at the second stage of aging. The supersaturation of Ni can be attributed to the extremely high cooling rates and thermal gradients experienced by the alloys after the L-PBF process,[7] which made the solution annealing step unnecessary for Ni_4Ti_3 precipitation. The nucleation of Ni_4Ti_3 is likely to occur not only at the grain and subgrain boundaries but also at oxide interfaces, oxide particles being of Ni_4Ti_3O or Ti_4Ni_2O type (Figure 16). Particle local inhomogeneities in terms of distribution and location sites strongly depend on the short aging times (15 min). This microstructure aspect was partially overcome by increasing aging temperature from 400 °C to 500 °C, as documented by the TEM inspections and, in particular, as reported in Figure 17.

With the increase in aging time, or aging temperature, the Ni_4Ti_3 precipitates keep growing at grain and subgrain boundaries and in the grain interior. The particle coarsening typically progresses along the coherent B2 matrix interface. The Ni_4Ti_3 particle coarsening proceeds by absorbing Ni atoms from the B2 matrix around them. This explains the increasing of TTs temperature found for DA samples (see Figure 1 and Table III).

Figure 17 shows heterogeneous nucleation of Ni_4Ti_3 phase precipitates as an important factor in the early stages of direct aging, especially in the higher temperature of 500 °C. It appears that precipitation of small lenticular Ni_4Ti_3 particles only occurs at and near grain and subgrain boundaries, as well as at oxide particle locations. Anyway, especially in the DA 400 °C alloy, vast portions of the grains appear free of precipitates. Only increasing the aging temperature to 500 °C, Ni_4Ti_3 precipitation become significant, and particles start coarsening even after the short aging time of 15 min. The higher volume fraction of Ni_4Ti_3 after direct aging at 500 °C promoted the greater formation of R-phase.

A further interesting aspect refers to the coherency/semi-coherency and non-coherency of the Ni_4Ti_3 phase to the B2 austenite matrix at the two aging temperatures. That is, in the DA 400 °C sample, Ni_4Ti_3 are mostly coherent and semi-coherent, with a low fraction of incoherent particles, while in DA 500 °C coherent, semi-coherent, and incoherent particles equally coexist.

The effects of these precipitates on the superelastic features of the samples are complex. Firstly, their presence in the heat-treated alloys was found to increase the TTs by reducing the Ni content of the matrix (see Figure 1 and Table III). This allowed the stress-induced martensitic transformation to happen at RT and 37 °C for these samples. On the other hand, in fact, for the as-built alloy both RT and 37 °C are much higher than A_f (– 16 °C), and the superelastic behavior is not appreciable. It is therefore reasonable to assume that the stress-induced martensite formation is impeded at these temperatures, which could be due to the fact that the stress required for its formation is higher than those reached during the compression tests, or to the exceeding of the martensite-destruct temperature (M_d).[17,71,72]

Another aspect to consider is that Ni_4Ti_3 precipitates act as nucleation sites for martensite as the load is applied, thus promoting the stress-induced martensitic transformation.[17,22,57] In this regard, the higher volume fraction of precipitates found in the DA 500 °C sample explains the lower σ_{PE} recorded during compression tests respect to DA 400 °C (Figures 8b and 10b). In fact,

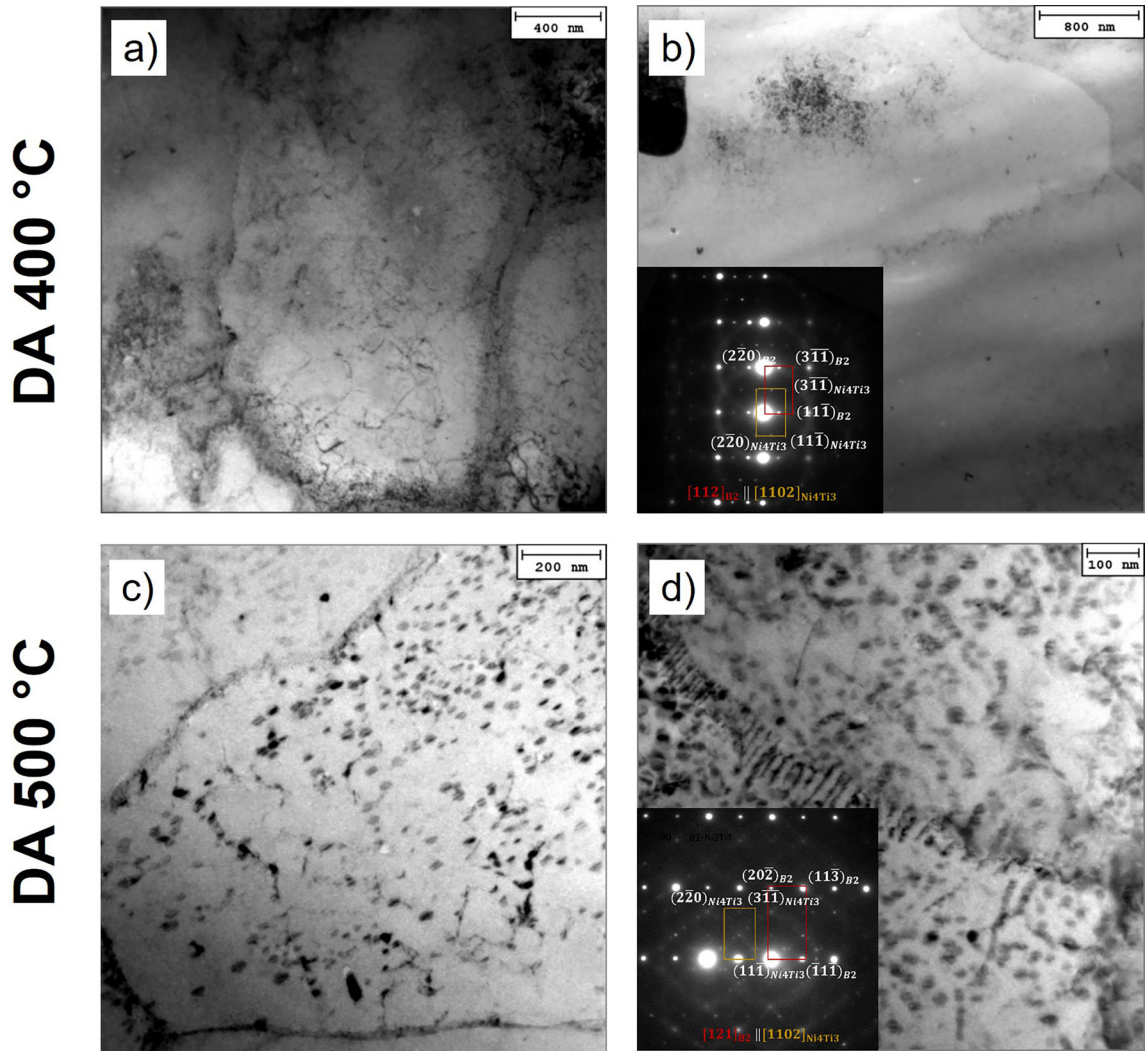

Fig. 17—Ni_4Ti_3 phase particles detected in: (*a*, *b*) DA 400 °C, (*c*, *d*) DA 500 °C.

at the interface between coherent Ni_4Ti_3 particles and B2 matrix, a coherent stress field is generated, which makes the transformation happen near these regions to relax the coherent stresses.[65]

Lastly, Ni_4Ti_3 precipitates are also known to increase the critical stress for the slip deformation mechanism (σ_{SLIP}) due to their precipitation hardening effect. In this way, since the chance of the occurring of plastic deformation is decreased, the stress-induced martensitic transformation necessary for SE is promoted.[9,11,73]

2. *Microhardness and compression up to failure*

Vickers microhardness results of the direct aged samples compared to the as-built are reported in Figure 19. It should be mentioned that hardness of NiTi is complex and strongly dependent on the temperature and the exhibited phases. Moreover, during hardness test, stress-induced transformations or variant reorientation can happen, as well as the formation of dislocations.[53]

Both the performed direct aging treatments increase the microhardness compared to the as-built sample, with a slightly decreasing trend with aging temperature, which is also in agreement with the literature.[19,74] In detail, hardness increases from 344 ± 23 HV to 437 ± 27 HV by direct aging at 400 °C and then decreases to 410 ± 16 HV by direct aging at 500 °C. The austenitic phase in NiTi has higher hardness than martensite.[50,53,75] Therefore, the higher hardness measured for direct aged alloys compared to the as-built is imputable to the presence of Ni_4Ti_3 precipitates and their precipitation hardening effect. It is in fact commonly known that hardness is strongly affected by the presence of precipitates, with a complex dependence on their size and distance.

Several reasons could explain the slightly lower hardness found after direct aging at 500 °C. Firstly, it may be ascribed to the precipitates dimension which was found to grow and consequently some become incoherent (Figure 18), which may have contributed to slightly decrease hardness.[74,76] Another explanation can be found by referring to the σ_{PE} parameter. In fact, for superelastic materials, a higher σ_{PE} corresponds to a higher force that can be recovered without causing a permanent deformation. Therefore, since DA 400 °C

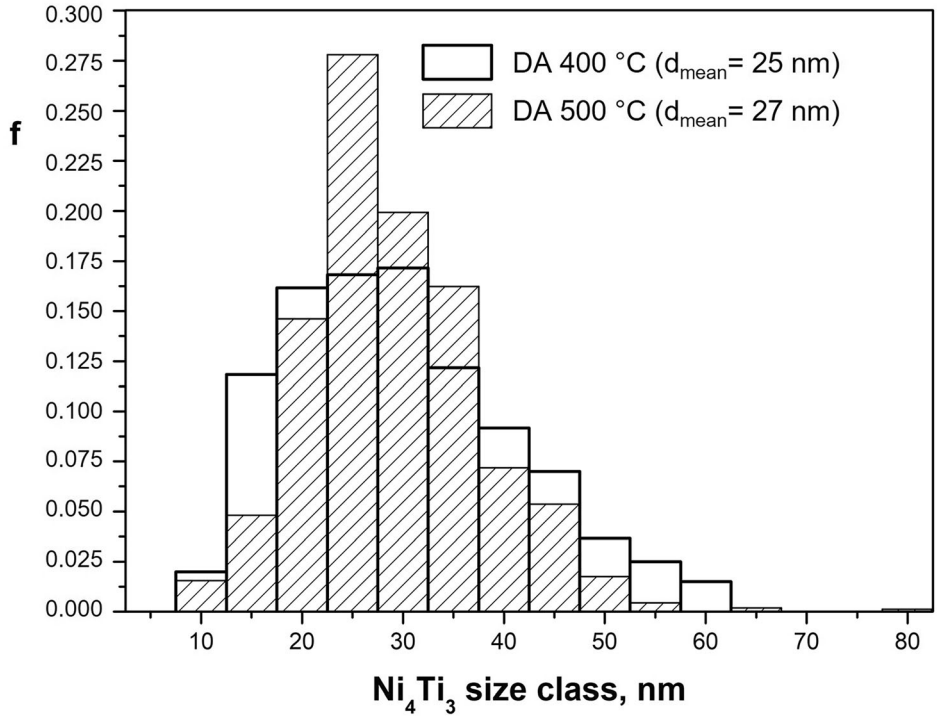

experimental condition	d_{av} (nm)	λ (nm)	f_V (%)
DA 400 °C	25 ± 3	134 ± 6	2.4 ± 0.8
DA 500 °C	27 ± 2	88 ± 6	12 ± 3

Fig. 18—Ni_4Ti_3 size distribution and statistic evaluation: mean size (d_{av}), mean edge-to-edge spacing (λ), volume fraction (f_V).

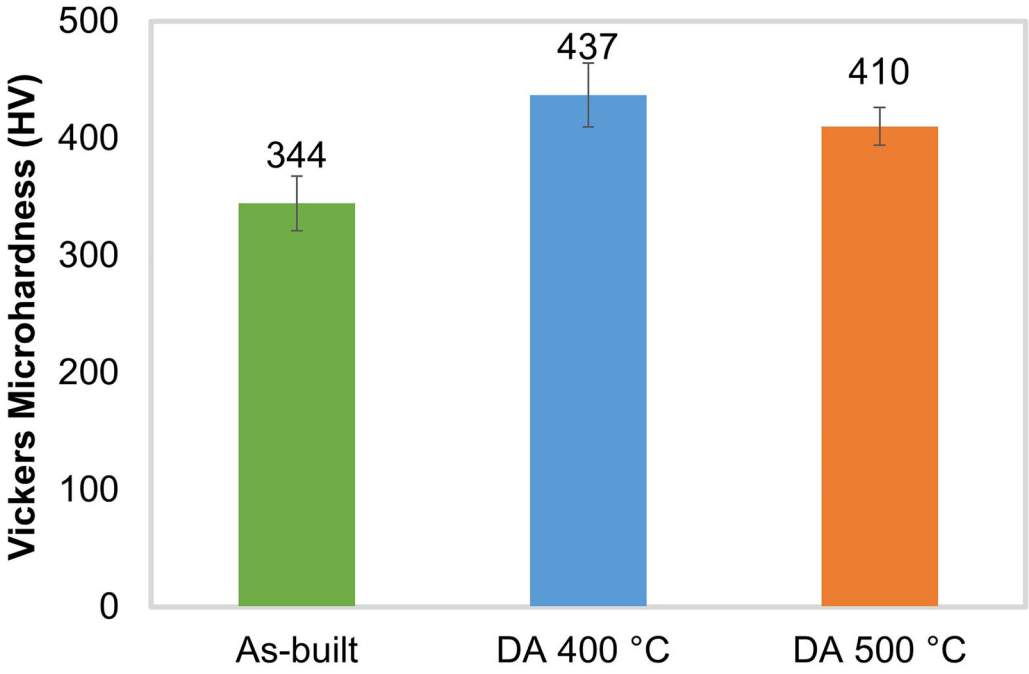

Fig. 19—Vickers microhardness of as-built, DA 400 °C and DA 500 °C samples.

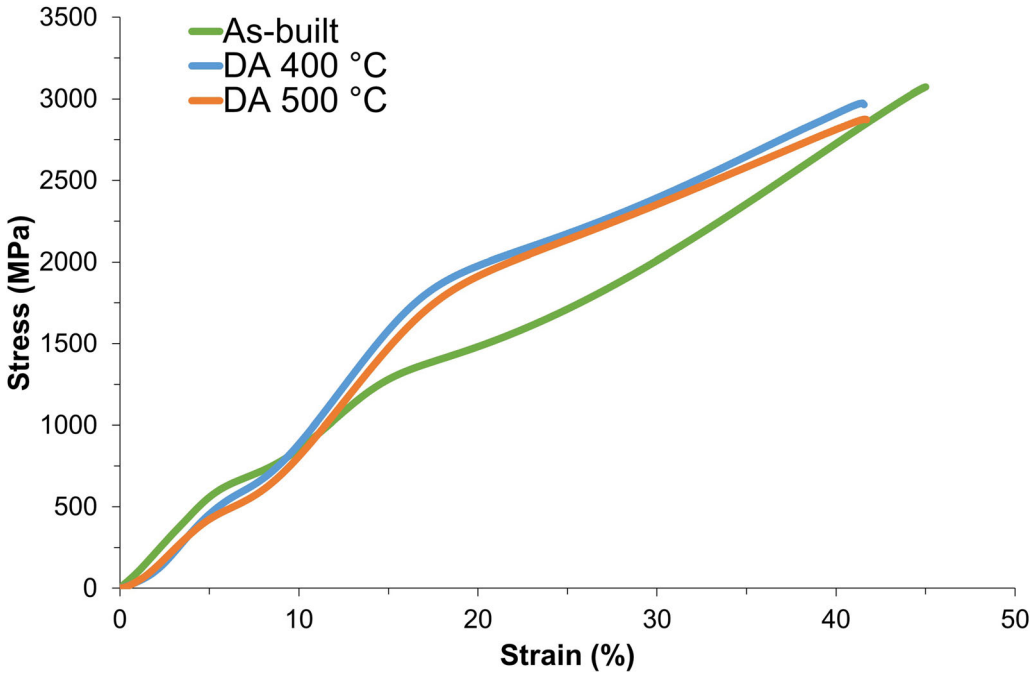

Fig. 20—Stress-strain plots for as-built and direct aged samples loaded until failure at RT.

exhibits the greatest σ_{PE} (Figures 8b and 10b), it will result in a lower permanent deformation and thus in a smaller indentation and higher Vickers hardness.[77] This only applies to material exhibiting superelastic responses, such as the direct aged samples, while it is not valid for the as-built condition.

Since hardness is commonly recognized as an indication of the strength and is mainly concerned to the plastic behavior of the material, compression tests until failure at RT were performed to deeply understand the mechanical behavior of direct aged alloys. Figure 20 reports the results of the complete compression tests.

The first region of the curves is related to the elastic deformation of the initial structure, *i.e.* austenite for the as-built sample and austenite and martensite for the direct aged samples. By loading up to the first inflection point of each curve, which corresponds to σ_{PE}, stress-induced martensite forms from austenite. Then, a decrease in slope occurs between 5 pct and 8 pct of strain. Up to this point, the behavior of samples reflects what previously found during cyclic and incremental compressive tests (Figures 7 and 9): the as-built sample shows higher σ_{PE}, as well as higher stress at the same strain value, followed by DA 400 °C and DA 500 °C. After, the formed martensite is firstly elastically and then plastically deformed up to failure. The plastic deformation by dislocation slip takes place as the stress reaches σ_{SLIP}, that is the critical stress for the slip deformation mechanism and corresponds to the second inflection point of the curve.[78] Beyond this point, at the same strain value, both the direct aged alloys reach higher stresses compared to the as-built condition. This is consistent with the hardness results reported in Figure 19. It should be noted that in this region all the samples present the same phase (*i.e.* martensite), and therefore the hardening effect of direct aged alloys with respect to the as-built can be attributed to the presence of Ni_4Ti_3 precipitates and to their precipitation hardening effect. It is therefore evident that Ni_4Ti_3 phase increased σ_{SLIP} in the direct aged samples. Lastly, the Ni_4Ti_3 precipitates present in the DA samples lead to a slight reduction of both the stress and strain at failure compared to the as-built alloy. This is due to the precipitation hardening effect of Ni-rich phases and to their brittle nature.[17,79]

IV. CONCLUSIONS

Direct aging heat treatments were performed at 400 °C and 500 °C for a short exposure time of 15 min on NiTi samples produced by laser powder bed fusion. Their properties were compared to those of samples that underwent the traditional treatment involving solution annealing and aging.

Cyclic compression tests were carried out to characterize the superelastic behavior. All the heat-treated samples showed negligible residual strain values after 15 cycles up to 6 pct of deformation. After 10 cycles of incremental deformation from 1 to 10 pct, the total cumulative strain was found to be lower than 2 pct. This, together with the high stability exhibited during compression cycles, proves the achievement of the superelastic effect up to 10 pct of strain for all the heat-treated alloys. The solution treatment was found to be not required to reach superelasticity due to the comparable results obtained with and without this step.

Ni_4Ti_3 precipitates were found after both the direct aging heat treatments. The alloy direct aged at 500 °C showed a significantly higher precipitation of Ni_4Ti_3

phase particles compared to the one direct aged at 400 °C. Moreover, the large presence of this phase after direct aging at 500 °C promoted the greater formation of R-phase at the B19' martensite lath boundaries. On the other hand, martensite volume fraction was higher in the alloy direct aged at 400 °C compared to samples treated at 500 °C.

Direct aged alloys resulted in higher microhardness compared to the as-built, due to the presence of Ni_4Ti_3 phase and the resulting precipitation hardening effect. Ni_4Ti_3 precipitates were also found to enhance the critical stress at which the slip plastic deformation occurs, as well as the resistance during plastic deformation for both the direct aged alloys.

Lastly, the superelastic features of direct aged alloys are preserved during compression tests at 37 °C. Short-time direct aging heat treatments at 400 °C and 500 °C can thus be exploited to enhance properties of NiTi components intended for biomedical applications.

ACKNOWLEDGMENTS

The authors deeply thank Dr. Karthikeyan Tamilselvam (Dublin City University) for printing samples, Prof. Stefano Pandini, Mrs. Gloria Spagnoli and Mrs. Isabella Peroni (University of Brescia) for running DSC tests, Dr. Annalisa Zacco, Chemistry for Technologies Laboratory (University of Brescia) and INSTM RU of Brescia for XRD measurements, Dr. Diego Paderno (University of Brescia) for preparing the compression samples and Dr. Lorenzo Montesano (University of Brescia) for the SEM analysis and technical support in the experimental activities.

FUNDING

Open access funding provided by Università degli Studi di Brescia within the CRUI-CARE Agreement. This publication has emanated from research supported by a research grant from Science Foundation Ireland (SFI) under grant number 16/RC/3872 and is co-funded by the European Regional Development Fund. For the purpose of Open Access, the author has applied a CC BY public copyright license to any Author Accepted Manuscript version arising from this submission.

CONFLICT OF INTEREST

On behalf of all authors, the corresponding author states that there is no conflict of interest.

OPEN ACCESS

REFERENCES

1. M.H. Elahinia, M. Hashemi, M. Tabesh, and S.B. Bhaduri: *Progr. Mater. Sci.*, 2012, vol. 57, pp. 911–46.
2. J. Van Humbeeck: *Mater. Sci. Eng. A*, 1999, vol. 273–275, pp. 134–48.
3. K. Otsuka and C.M. Wayman: *Shape Memory Materials*, Cambridge University Press, Cambridge, 1998.
4. C.M. Wayman and T.W. Duerig: *Engineering Aspects of Shape Memory Alloys*, Butterworth-Heinemann Ltd, Oxford, 1990, pp. 3–20.
5. E. Farber, J.N. Zhu, A. Popovich, and V. Popovich: *Mater. Today*, 2020, vol. 30, pp. 761–67.
6. T. Habu: *Shape Memory Alloys for Biomedical Applications*, Woodhead Publishing Limited, Cambridge, 2008, pp. 86–100.
7. T. DebRoy, H.L. Wei, J.S. Zuback, T. Mukherjee, J.W. Elmer, J.O. Milewski, A.M. Beese, A. Wilson-Heid, A. De, and W. Zhang: *Progr. Mater. Sci.*, 2018, vol. 92, pp. 112–224.
8. Z.X. Khoo, Y. Liu, J. An, C.K. Chua, Y.F. Shen, and C.N. Kuo: *Materials*, 2018, vol. 11, p. 519.
9. K. Safaei, H. Abedi, M. Nematollahi, F. Kordizadeh, H. Dabbaghi, P. Bayati, R. Javanbakht, A. Jahadakbar, M. Elahinia, and B. Poorganji: *JOM*, 2021, vol. 73, pp. 3771–86.
10. T. Saburi, T. Tatsumi and S. Nenno: *J. Phys. (Paris), Colloque C4*, 1982, vol. 43, pp. c4261–66.
11. K. Otsuka and X. Ren: *Progr. Mater. Sci.*, 2005, vol. 50, pp. 511–678.
12. H. Shahmir, M. Nili-Ahmadabadi, and F. Naghdi: *Mater. Des.*, 2011, vol. 32, pp. 365–70.
13. P.R. Halani, I. Kaya, Y.C. Shin, and H.E. Karaca: *Mater. Sci. Eng. A*, 2013, vol. 559, pp. 836–43.
14. J. Lee and Y.C. Shin: *Lasers Manuf. Mater. Process.*, 2019, vol. 6, pp. 41–58.
15. J. Dutkiewicz, Ł Rogal, D. Kalita, M. Węglowski, S. Błacha, K. Berent, T. Czeppe, A. Antolak-Dudka, T. Durejko, and T. Czujko: *J. Mater. Eng. Perform.*, 2020, vol. 29, pp. 4463–73.
16. B. Lu, X. Cui, M. Dong, W. Ma, and G. Jin: *J. Mater. Eng. Perform.*, 2020, vol. 29, pp. 2491–98.
17. C. Haberland, H. Meier and J. Frenzel: *ASME 2012 Conf. Smart Mater., Adapt. Struct. Intell. Syst., Proc., SMASIS 2012*, 2012, pp. 97–104.
18. S. Saedi, A.S. Turabi, M.T. Andani, C. Haberland, H. Karaca, and M. Elahinia: *J. Alloys Compd.*, 2016, vol. 677, pp. 204–10.
19. S. Saedi, A.S. Turabi, M.T. Andani, N.S. Moghaddam, M. Elahinia, and H.E. Karaca: *Mater. Sci. Eng. A*, 2017, vol. 686, pp. 1–10.
20. S. Saedi, N. S. Moghaddam, A. Amerinatanzi, M. Elahinia and H. E. Karaca: *Acta Mater.*, 2018, vol. 144, pp. 552–560.
21. K. Khanlari, Q. Shi, K. Li, K. Hu, P. Cao, and X. Liu: *Intermetallics*, 2021, vol. 131, 107088.
22. G. Carlucci, L. Patriarca, A. G. Demir, J. N. Lemke, A. Coda, B. Previtali and R. Casati: *Shape Mem. Superelast.*, 2022, vol. 8, pp. 235–47 (2022).
23. J.C. Chekotu, R. Groarke, K. O'Toole, and D. Brabazon: *Materials*, 2019, vol. 12, p. 809.
24. M. H. Elahinia, N. S. Moghaddam, M. T. Andani, A. Amerinatanzi, B. A. Bimber and R. F. Hamilton: *Progr. Mater. Sci.*, 2016, vol. 83, pp. 630–63.

25. R. Casati, M.H. Nasab, M. Coduri, V. Tirelli, and M. Vedani: *Metals*, 2018, vol. 8, p. 11.
26. H. Zhang, Y. Wang, J.J. Wang, D.R. Ni, D. Wang, B.L. Xiao, and Z.Y. Ma: *J. Mater. Sci. Technol.*, 2022, vol. 108, pp. 226–35.
27. H. Tang, C. Gao, Y. Zhang, N. Zhang, C. Lei, Y. Bi, P. Tang, and J.H. Rao: *J. Mater. Sci. Technol.*, 2023, vol. 139, pp. 198–209.
28. M.S. Baek, R. Kreethi, T.-H. Park, Y. Sohn, and K.-A. Lee: *Mater. Sci. Eng. A*, 2021, vol. 819, p. 141486.
29. X. Zhang and H. Sehitoglu: *Mater. Sci. Eng. A*, 2004, vol. 374, pp. 292–302.
30. K. Khanlari, M. Ramezani, P. Kelly, P. Cao, and T. Neitzert: *Intermetallics*, 2018, vol. 100, pp. 32–43.
31. K.N. Melton: *Engineering Aspects of Shape Memory Alloys*, Butterworth-Heinemann, Oxford, 1990, pp. 21–35.
32. J. Khalil-Allafi, A. Dlouhy, and G. Eggeler: *Acta Mater.*, 2002, vol. 50, pp. 4255–74.
33. T.W. Duerig and K. Bhattacharya: *Shape Mem. Superelast.*, 2015, vol. 1, pp. 153–61.
34. X. Ren, N. Miura, J. Zhang, K. Otsuka, K. Tanaka, M. Koiwa, T. Suzuki, Y.I. Chumlyakov, and M. Asai: *Mater. Sci. Eng. A*, 2001, vol. 312, pp. 196–206.
35. Y. Zheng, F. Jiang, L. Li, H. Yang, and Y. Liu: *Acta Mater.*, 2008, vol. 56, pp. 736–45.
36. K. Kazemi-Choobi, J. Khalil-Allafi, and V. Abbasi-Chianeh: *J. Alloys Compd.*, 2014, vol. 582, pp. 348–54.
37. E. Henderson, D.H. Nash, and W.M. Dempster: *J. Mech. Behav. Biomed. Mater.*, 2011, vol. 4, pp. 261–68.
38. H. Sitepu: *Powder Diffr.*, 2009, vol. 24, pp. 315–26.
39. A. Chmielewska, B. Wysocki, P. Kwaśniak, M.J. Kruszewski, B. Michalski, A. Zielińska, B. Adamczyk-Cieślak, A. Krawczyńska, J. Buhagiar, and W. Święszkowski: *Materials*, 2022, vol. 15, p. 3304.
40. Y. Kudoh, M. Tokonami, S. Miyazaki, and K. Otsuka: *Acta Metall.*, 1985, vol. 33, pp. 2049–56.
41. B. Bertheville, M. Neudenberger, and J.E. Bidaux: *Mater. Sci. Eng. A*, 2004, vol. 384, pp. 143–50.
42. J.C. Hey and A.P. Jardine: *Mater. Sci. Eng. A*, 1994, vol. 188, pp. 291–300.
43. B.Y. Li, L.J. Rong, X.H. Luo, and Y.Y. Li: *Metall. Mater. Trans. A*, 1999, vol. 30A, pp. 2753–56.
44. S.M. Green, D.M. Grant, and N.R. Kelly: *Powder Metall.*, 1997, vol. 40, pp. 43–47.
45. M. Neikter, A. Huang, and X. Wu: *Int. J. Adv. Manuf. Technol.*, 2019, vol. 104, pp. 1381–91.
46. T. Bormann, B. Müller, M. Schinhammer, A. Kessler, P. Thalmann, and M. de Wild: *Mater Charact*, 2014, vol. 94, pp. 189–202.
47. L. Xue, K.C. Atli, S. Picak, C. Zhang, B. Zhang, A. Elwany, R. Arroyave, and I. Karaman: *Acta Mater.*, 2021, vol. 215, p. 117017.
48. S.E. Saghaian, M. Nematollahi, G. Toker, A. Hinojos, N.S. Moghaddam, S. Saedi, C.Y. Lu, M.J. Mahtabi, M.J. Mills, M. Elahinia, and H.E. Karaca: *Opt. Laser Technol.*, 2022, vol. 149, p. 107680.
49. N.S. Moghaddam, S. Saedi, A. Amerinatanzi, A. Hinojos, A. Ramazani, J. Kundin, M.J. Mills, H. Karaca, and M. Elahinia: *Sci. Rep.*, 2019, vol. 9, p. 41.
50. M. Zamani, M. Kadkhodaei, M. Badrossamay and E. Foroozmehr: *J. Intell. Mater. Syst. Struct.*, 2021, pp. 1-12.
51. J.N. Zhu, E. Borisov, X. Liang, R. Huizenga, A. Popovich, V. Bliznuk, R. Petrov, M. Hermans, and V. Popovich: *J. Mater. Sci.*, 2022, vol. 57, pp. 6066–84.
52. A. Poudel, M. S. Yasin, J. Ye, J. Liu, A. Vinel, S. Shao and N. Shamsaei: *Nat. Commun.*, 2022, vol. 13.
53. A.S. Turabi, S. Saedi, S.M. Saghaian, H.E. Karaca, and M.H. Elahinia: *Shape Memory Alloy Actuators: Design, Fabrication and Experimental Evaluation*, Wiley, New York, 2016, pp. 239–77.
54. Y. Liu, Y. Liu, and J. Humbeeck: *Scr. Mater.*, 1998, vol. 39, pp. 1047–55.
55. Y. Liu, Z. Xie, J. Van Humbeeck, and L. Delaey: *Scr. Mater.*, 1999, vol. 41, pp. 1273–81.
56. P. Chowdhury, L. Patriarca, G. Ren, and H. Sehitoglu: *Int. J. Plast.*, 2016, vol. 81, pp. 152–67.
57. S.Y. Jiang, Y.Q. Zhang, Y.N. Zhao, S.W. Liu, L. Hu, and C.Z. Zhao: *Trans. Nonferrous Met. Soc. China (English Edition)*, 2016, vol. 25, pp. 4063–71.
58. A.R. Pelton, J. DiCello, and S. Miyazaki: *Minim. Invasive Ther. Allied Technol.*, 2000, vol. 9, pp. 107–18.
59. R.R. Adharapurapu and K.S. Vecchio: *Exp. Mech.*, 2007, vol. 47, pp. 365–71.
60. X. Huang and Y. Liu: *Scr. Mater.*, 2001, vol. 45, pp. 153–60.
61. S. Nemat-Nasser and W.G. Guo: *Mech. Mater.*, 2006, vol. 38, pp. 463–74.
62. M. Nishida, C.M. Wayman, R. Kainuma, and T. Honma: *Scripta Metall.*, 1986, vol. 20, pp. 899–904.
63. M. Nishida and C.M. Wayman: *Mater. Sci. Eng.*, 1987, vol. 93, pp. 191–203.
64. B. C. Hornbuckle, X. X. Yu, R. D. Noebe, R. Martens, M. L. Weaver and G. B. Thompson: *Mater. Sci. Eng. A*, 2015, vol. 639, pp. 336–44.
65. N. Zhou, C. Shen, M.F.X. Wagner, G. Eggeler, M.J. Mills, and Y. Wang: *Acta Mater.*, 2010, vol. 58, pp. 6685–94.
66. J.I. Kim and S. Miyazaki: *Acta Mater.*, 2005, vol. 53, pp. 4545–54.
67. W.H. Zou, X.D. Han, R. Wang, Z. Zhang, W.Z. Zhang, and J.K.L. Lai: *Mater. Sci. Eng. A*, 1996, vol. 219, pp. 142–47.
68. J. Khalil Allafi, X. Ren and G. Eggeler: *Acta Mater.*, 2002, vol. 50, pp. 793-803.
69. J. Michutta, C. Somsen, A. Yawny, A. Dlouhy, and G. Eggeler: *Acta Mater.*, 2006, vol. 54, pp. 3525–42.
70. A. Dlouhý, O. Bojda, C. Somsen, and G. Eggeler: *Mater. Sci. Eng. A*, 2008, vol. 481–482, pp. 409–13.
71. T. Saburi: *Shape Memory Materials*, Cambridge University Press, Cambridge, 1999, pp. 49–96.
72. K. Otsuka and C.M. Wayman: *Shape Memory Materials*, Cambridge University Press, Cambridge, 1999, pp. 27–48.
73. S. Miyazaki, Y. Ohmi, K. Otsuka and Y. Suzuki: *J. Phys.* (*Paris*), 1982, vol. 43, pp. c4.255-c254.260.
74. H.E. Karaca, S.M. Saghaian, G. Ded, H. Tobe, B. Basaran, H.J. Maier, R.D. Noebe, and Y.I. Chumlyakov: *Acta Mater.*, 2013, vol. 61, pp. 7422–31.
75. X. Huang, J. Nohava, B. Zhang, and A.G. Ramirez: *Int. J. Smart Nano Mater.*, 2011, vol. 2, pp. 39–49.
76. K. Gall, K. Juntunen, H.J. Maier, H. Sehitoglu, and Y.I. Chumlyakov: *Acta Mater.*, 2001, vol. 49, pp. 3205–17.
77. M.J. Mahtabi, A. Yadollahi, M. Rahmati, and T.W. Stone: *Arabian J. Sci. Eng.*, 2018, vol. 43, pp. 5029–33.
78. H. Hosoda and T. Inamura: *Shape Memory Alloys for Biomedical Applications*, Woodhead Publishing, Sawston, 2009, pp. 20–36.
79. J. Mentz, M. Bram, H.P. Buchkremer, and D. Stöver: *Mater. Sci. Eng. A*, 2008, vol. 481–482, pp. 630–34.